Monthly Notices
of the
ROYAL ASTRONOMICAL SOCIETY

MNRAS **462,** 610–635 (2016) doi:10.1093/mnras/stw1572
Advance Access publication 2016 July 1

Rings and arcs around evolved stars – I. Fingerprints of the last gasps in the formation process of planetary nebulae

G. Ramos-Larios,[1★] E. Santamaría,[1] M. A. Guerrero,[2★] R. A. Marquez-Lugo,[2] L. Sabin[3★] and J. A. Toalá[2,4]

[1]Instituto de Astronomía y Meteorología, CUCEI, Universidad de Guadalajara, Av. Vallarta No. 2602, Col. Arcos Vallarta, 44130 Guadalajara, Jalisco, Mexico
[2]Instituto de Astrofísica de Andalucía, IAA-CSIC, C/Glorieta de la Astronomía s/n, E-18008 Granada, Spain
[3]Instituto de Astronomía, Universidad Nacional Autónoma de México, Apdo. Postal 877, 22860 Ensenada, B. C., Mexico
[4]Institute of Astronomy and Astrophysics, Academia Sinica (ASIAA), Taipei 10617, Taiwan

Accepted 2016 June 29. Received 2016 June 24; in original form 2015 November 3

ABSTRACT

Evolved stars such as asymptotic giant branch stars (AGB), post-AGB stars, proto-planetary nebulae (proto-PNe), and planetary nebulae (PNe) show rings and arcs around them and their nebular shells. We have searched for these morphological features in optical *Hubble Space Telescope* and mid-infrared *Spitzer Space Telescope* images of ∼650 proto-PNe and PNe and discovered them in 29 new sources. Adding those to previous detections, we derive a frequency of occurrence ≃8 per cent. All images have been processed to remove the underlying envelope emission and enhance outer faint structures to investigate the spacing between rings and arcs and their number. The averaged time lapse between consecutive rings and arcs is estimated to be in the range 500–1200 yr. The spacing between them is found to be basically constant for each source, suggesting that the mechanism responsible for the formation of these structures in the final stages of evolved stars is stable during time periods of the order of the total duration of the ejection. In our sample, this period of time spans ≲4500 yr.

Key words: techniques: image processing – stars: AGB and post-AGB – planetary nebulae: general – infrared: ISM.

1 INTRODUCTION

A significant fraction of low- and intermediate-mass evolved stars, i.e. asymptotic giant branch (AGB) stars, post-AGB stars, proto-planetary nebulae (proto-PNe), and planetary nebulae (PNe), are characterized by external structures such as knots, ansae, jets, haloes, arcs, and complete rings (see e.g. Balick & Frank 2002). The formation of the aforementioned features is connected with the mass-loss processes occurring at the late evolutionary stages of these objects.

The nebular shells are mainly composed of three different structures: an inner rim, formed by the collision of the current fast stellar wind with the AGB envelope; an outer shell, produced by the passage through the AGB envelope of a D-type front due to the pressure difference between ionized and neutral material (Mellema 1994); and a halo, which can be attributed to final mass-loss episodes common in the subsequent phases of the AGB (Balick et al. 1992) and are followed by the 'flash' ionization of the AGB envelope (Mellema 1994; Corradi et al. 2003; Perinotto et al. 2004).

Several theoretical and observational works have been pursued to establish the global properties of these haloes commonly surrounding PNe (e.g. Chu, Jacoby & Arendt 1987; Corradi et al. 2003). There is a general agreement on the association of these haloes with a major mass-loss episode occurring during the last thermal pulse (TP; Stanghellini & Pasquali 1995; Villaver, García-Segura & Manchado 2002a). In this scenario, the haloes of PNe provide information on the mass-loss rates and interpulse periods of the last TPs during the late AGB evolution (e.g. Stanghellini & Pasquali 1995; Hajian et al. 1997), provided the observational data are correctly modelled (Villaver, Manchado & García-Segura 2002b).

It has been reported more recently the detection of annular intensity enhancements in the region between the nebular shell and the outer halo of several PNe which are commonly referred to as rings or arcs. First reported by Terzian & Hajian (2000), these features were described as reflection traits in the layers of proto-PNe, where the neutral material is predominant. There is also further evidence that these features seem to emerge in spherical symmetry from the outflowing dust, e.g. CRL 2688 (Sahai et al. 1998), IRAS 17150−3224 (Kwok, Su & Hrivnak 1998), IRAS 17441−2411 (Su et al. 1998), and IRAS 20028+3910 (Hrivnak, Kwok & Su 2001). However, it should be noted that concentric arcs are found in the ionized haloes of older PNe (Terzian & Hajian 2000; Corradi et al.

★ E-mail: gerardo@astro.iam.udg.mx (GR-L); mar@iaa.es (MAG); lsabin@astrosen.unam.mx (LS)

2004). The nature of these features is unclear. They can be interpreted as the projection of spherical bubbles or shells on to the plane of the sky, whose origin is associated with periodic isotropic nuclear mass pulsations (Balick, Wilson & Hajian 2001; Kwok 2001). In some cases, however, the ring-like features can be interpreted as the projection of two-dimensional rings, as those seen in Hb 12 (Kwok & Hsia 2007).

The properties of these features are rather uncertain, but what is clear is their faintness, with values lower than ∼15 per cent of surface brightness as compared against the main envelopes (Corradi et al. 2004). The only source with a higher value is Hb 5, whose ratio is close to 1. Moreover, the enhancement of the rings has been calculated compared to the inter-ring regions and vary from ∼2 (Kwok, Su & Stoesz 2001) up to ∼10 (Mauron & Huggins 1999). Besides these general properties, only the rings of one PN, NGC 6543, have been reported in detail (Balick et al. 2001; Hyung et al. 2001). One of the main results of both studies is the relative electron temperatures found in the inter-ring regions. Where Balick et al. (2001) determined temperatures relatively normal (although atypical line-widths), Hyung et al. (2001) found larger temperatures. The high electron temperature, if confirmed, might be linked to the physical processes involved in the formation of the rings.

The origin of these features is also rather uncertain. They are part of the AGB envelope, suggesting that the AGB wind is not completely steady towards the end of the AGB phase, but that the outflow has quasi-periodic oscillations in mass-loss rate or velocity. The time-scale for these oscillations is estimated to be a few hundred years. This time-scale, however, is too long to be the result of stellar pulsation, with periods of a few hundred days, but too short to be due to nuclear TPs, which occur once in 10^4–10^5 yr (Simis, Icke & Dominik 2001). In a few cases, a spiral pattern has been detected, which is interpreted as the result of the interaction of the AGB wind with a binary companion (Kim & Taam 2012a; Maercker et al. 2012).

Simis et al. (2001) present a model where the viscous momentum is transferred between the gas and grains. They predict that the grains drift could lead to quasi-periodic winds on the AGB phase. Grain drift become an essential part for variations in the mass-loss rate. Another similar scenario is proposed by Mastrodemos & Morris (1999). In this case, the dust drift velocity show the behaviour expected on the basis of complete momentum coupling and increases from the equator to high latitudes. A further interesting feature is about regions where the grains are responsible for polycyclic aromatic hydrocarbon (PAH) bands or dust continuum, where the rings in the infrared (IR) might be in a different position from the gas in the same region as probed by narrow-band Hα, [N II] or [O III] images. *Spitzer Space Telescope* (*SST*) images show that the 3.6 and 4.5 μm emissions are associated with gaseous components of emission in many PNe (e.g. Hora et al. 2004; Ramos-Larios & Phillips 2008), whereas the 5.8 and 8.0 μm emissions are mainly dominated by PAH bands of small dust grains.

With the purpose to assess the presence of concentric brightness enhancements around and outside the main nebular shells of proto-PNe and PNe and to study their nature, we have undertaken an extensive investigation of high-quality images available in the *Hubble Space Telescope* (*HST*) and *SST* archives. These have revealed the presence of ring-like features and arcs in a significant number of sources, basically doubling the number of previous detections. The observations and archival data are presented in Section 2. The data analysis and the results are described in Sections 3 and 4, respectively. The discussion is presented in Section 5 and a final summary is given in Section 6.

2 OBSERVATIONS AND ARCHIVAL DATA

2.1 *HST* optical and near-IR imaging

The observations analysed in this paper were obtained using the Wide Field Planetary Camera 2 (WFPC2; Biretta et al. 2008), the Wide Field and Planetary Camera 3 (WFC3; Dressel 2015), the Advanced Camera for Surveys (ACS; Avila et al. 2015), and the Near Infrared Camera and Multi-Object Spectrometer (NICMOS; Thatte et al. 2009). The observations, acquired through a variety of filters, with different exposure times and at different dates, correspond to the *HST* observing programmes with Prop. ID 11122 (PI: B. Balick), 6119 (PI: H. Bond), 6364 (PI: M. Bobrowsky), 6347 (PI: K. Borkowski), 9839 (PI: D. Garnett), 8773 (PI: A. Hajian), 5403 (PI: J. Harrington), 8210 (PI: B. Hrivnak), 8307 (PI: S. Kwok), 6737, 10627 (PI: M. Meixner), 9314, 11090 (PI: K. Noll), 11331 (PI: N. Pirzkal), 6353, 8345, 9463, 10536 and 10851 (PI: R. Sahai), 11657 (PI: L. Stanghellini), 10807 (PI: M. Stute), 6221 (PI: J. Trauger), and 9356 (PI: A. Zijlstra). Many of the images were obtained in snapshot mode, i.e. with short integration times. All images were pipeline reduced and retrieved from the Mikulski Archive for Space Telescopes (MAST) and the Hubble Legacy Archive[1] at the Space Telescope Science Institute (STScI).[2]

The main narrow-band filters used were the [N II], Hα, and [O III]. Images through the WFC3 broad-band filters *F*200*LP* and *F*350*LP* were also used. For some objects, only images obtained through broad-band filters such as the *F*410*M*, *F*435*W*, *F*547*M*, *F*555*W*, *F*606*W*, *F*625*W*, and *F*814*W* filters were available. All filters characteristics and instruments are listed in Table 1.

2.2 Ground-based imaging

We obtained narrow-band images of IC 3568 in the Hα, [N II], and [O III] emission lines. The images were acquired on 2009 June 21 using the Andalucia Faint Object Spectrograph and Camera (ALFOSC) mounted on the 2.56-m Nordic Optical Telescope (NOT) at the Observatorio de El Roque de los Muchachos in La Palma, Spain. A 2048 × 2048 E2V CCD was used as detector. Its pixel size of 13.5 μm implies a plate scale of 0.184 arcsec pixel^{-1}, resulting in a field of view (FoV) of 6.3 arcmin × 6.3 arcmin. The central wavelengths and bandwidths of the filters are listed in Table 1. The seeing was ∼0.7 arcmin, as measured from stars in the FoV.

Two frames with integration times of 450 s were taken for each filter, leading to total exposure times of 900 s. The data were bias-subtracted and flat-fielded using twilight flats employing standard IRAF[3] routines.

2.3 Mid-IR imaging

The *Spitzer* Infrared Array Camera (IRAC; Fazio et al. 2004) images of PNe were downloaded from the NASA/IPAC Infrared Science

[1] http://hla.stsci.edu/

[2] STScI is operated by the Association of Universities for Research in Astronomy, Inc., under NASA contract NAS5-26555.

[3] IRAF, the Image Reduction and Analysis Facility, is distributed by the National Optical Astronomy Observatory, which is operated by the Association of Universities for Research in Astronomy (AURA) under cooperative agreement with the National Science Foundation.

Table 1. Telescopes and instrumentation.

Telescope	Instrument	Filter	λ_c (Å)	$\Delta\lambda$ (Å)
HST	ACS	*F*435*W*	4297	1038
		*F*606*W*	5907	2342
		*F*625*W*	6318	1442
		*F*658*N* [N II]	6584	78
		*F*814*W*	8333	2511
	WFC3	*F*200*LP*	2000	>8000
		*F*350*LP*	3500	>7000
		*F*502*N* [O III]	5010	65
		*F*814*W*	8353	2555
	WFPC2	*F*410*M*	4086	147
		*F*502*N* [O III]	5012	27
		*F*547*M*	5446	487
		*F*555*W*	5202	1223
		*F*606*W*	5767	1579
		*F*656*N* Hα	6564	22
		*F*658*N* [N II]	6591	29
		*F*814*W*	8203	1758
	NIC3	*F*160*W*	16 000	4000
NOT	ALFOSC	[O III]	5007	30
		Hα	6567	8
		[N II]	6588	9
Spitzer	IRAC	3.6 μm band	35 500	7500
		4.5 μm band	44 930	10 150
		5.8 μm band	57 310	14 250
		8 μm band	78 720	29 050

Archive. The images belong to Programmes 68, 'Studying Stellar Ejecta on the Large Scale Using SIRTF-IRAC' (PI: Giovanni Fazio) and 40020, 'The Extended Haloes of Planetary Nebulae' (PI: Giovanni Fazio), and were obtained at different dates on 2004 and 2007, respectively.

The resulting images have been processed as described in the IRAC Instrument Handbook Version1.0.[4] The resulting post-Basic Calibrated Data are relatively free from artefacts and have been flux calibrated in units of MJy sr^{-1}. The background emission in these images is reasonably flat. The isophotal wavelengths and bandwidths of the filters used in these observations are listed in Table 1. The nominal spatial resolution for this camera lies between 1.7 and 2.0 arcsec (Fazio et al. 2004).

3 DATA ANALYSIS

The visual inspection of *HST*, *SST*, and ground-based direct images has revealed faint outer features in the PNe and proto-PNe listed in Tables 2–4. Their low surface brightness (1/100 to 1/1000 that of the central nebula) and roundish morphology suggest that they might be interpreted as concentric rings and arcs. Next, Section 3.1 describes our data processing to emphasize these structures in order to allow us a better identification and description of their morphology and a more quantitative assessment of their characteristics such as their spacing and number. The possibility that these structures are artefacts of the telescope point spread function (PSF) needs to be carefully assessed too. This is discussed in Section 3.2.

[4] http://ssc.spitzer.caltech.edu/irac/iracinstrumenthandbook/IRAC_Instrument_Handbook.pdf

3.1 Emphasizing outer structures of PNe and proto-PNe

In order to emphasize the outer structures detected in the direct images of PNe and proto-PNe, these images have been processed following two different techniques. First, we have produced red giant branch pictures for each object using the unsharp masking technique. The unsharp mask technique simulates the effect of a true unsharp mask which involves subtracting a blurred (or smoothed) version of an image from itself. This is carried out by first creating a low-pass-filtered version of the image and then subtracting the blurred image from the original one. This leads to an apparent image 'sharpening' (Levi 1974). It also reduces the dynamical range between the bright main nebula and the much fainter ring-like structures in the envelope, as it averages out the surface brightness of large areas and enhances the contrast between neighbouring details.

Alternatively, the so-called sda (shift, divide and add) algorithm described by Corradi et al. (2004) has been applied to our data set of images. The sda algorithm employs a 'jitter' procedure, in which a source image is shifted by a certain number of pixels along four orthogonal directions. The pixel shift used for each source is listed in Tables 2–4. It is typically in the range between 2 and 7 pixels for *HST* images, but for IC 4406 where the application of this technique was not necessary, and 5 or 7 pixels for *SST* images. The original image is then divided by the four displaced images and the resulting ratio maps are added all together. This leads to the enhancement of the ring structure and to the effective removal of the underlying emission from the nebular envelope.

The use of unsharp and sda images is somehow complementary. The former preserves the nebular morphology and rich details in the *HST* images that the latter loses, whereas the sda images greatly enhance the presence of faint concentric outer features. Otherwise, the detection of faint outer structures by these two techniques reinforces their real presence in the images.

Finally, in order to investigate variations in emission due to these ring-like structures, radial profiles across selected positions were extracted from the sda images. The underlying, smoother component of emission from the nebular envelope is effectively removed by this technique, while keeping the information on the spatial distribution of ring-like structures. This procedure has allowed us to produce spatial profiles of the rings clean of the envelope emission. These have been used to assess the number of ring-like structures or arcs and the spacing between them listed in Tables 2–4.

The colour unsharp masking imaging, the sda images and sda spatial profiles of four selected sources with ring-like structures are shown in the top, middle, and bottom panels, respectively, of Figs 1–4. The images and spatial profiles of the remaining 27 objects with ring-like structures are shown in the Appendix arranged by their Galactic longitudes (Figs A1 to A25). The unsharp masking pictures have been made out from one, two, or three filters. When one filter is used, it is assigned a red palette. When two filters are used, the red palette is assigned to the filter with the longest wavelength, and the blue-green palette to the other filter. When three filters are used, similar scheme is used for the three independent palettes. The only exception to this scheme has been CRL 915, for which a different combination of colours better reinforces the outer structures (Appendix Fig. A12). The spatial profiles have been extracted along selected directions that emphasize the ring location. The extent of these spatial profiles has been limited to the nebular envelope section where ring-like features are seen in direct images. The sda profiles reveal a number of peaks and minima. To highlight the location of these features, a linear fit to the minima of these profiles has been obtained and subtracted from the sda profiles shown in the bottom panels of these figures.

Table 2. *HST* objects with new rings detection.

Object	PNG	RA (J2000)	Dec. (J2000)	Type	No. of rings	Spacing (arcsec)	Filter	sda shift (pix)	*d* (kpc)	Ref.
PM 1-255	027.5−00.8	18 44 41.71	−05 09 26.05	R	3	0.1–0.2	*F*606*W*	3	6.9±1.0	1
NGC 6572	034.6+11.8	18 12 06.36	+06 51 13.01	BR	5	0.4–0.8	[O III]	3	2.5±0.5	1
GLMP 870	035.2−02.6	19 05 02.06	+00 48 50.91	Ae	2	0.2	*F*606*W*	5	8.5±1.3	1
Vy 2-2	045.4−02.7	19 24 22.22	+09 53 56.29	R	4	0.5–0.6	Hα	3	2.7±0.6	1
Vy 1-2	053.3+24.0	17 54 22.98	+27 59 58.12	R	4	0.5–0.6	[O III]	7	5.0	2
BD+30°3639	064.7+05.0	19 34 45.23	+30 30 58.94	R/BR	5	0.8–1.3	Hα	5	1.25±0.25	1
PM 2-42	067.1+02.7	19 49 29.56	+31 27 16.22	Ae	3	0.2–0.3	*F*435*W*	5	1.18±0.28	1
HD 161796	077.1+30.8	17 44 55.46	+50 02 39.48	BR	3	0.8–1.0	*F*547*M*	5	1.36±0.30	1
IC 5117	089.8−05.1	21 32 30.97	+44 35 47.51	Ae	3	0.5	Hα	3	5.0±0.7	1
GLMP 1058	096.7−11.5	22 24 31.43	+43 43 10.90	R	4	0.4–0.5	*F*435*W*	7	4.3±0.6	1
GLMP 1059	103.3−02.5	22 29 10.37	+54 51 06.35	R	5	1.0–1.4	*F*555*W*	7	1.39±0.20	1
Hb 12[a]	111.8−02.8	23 26 14.82	+58 10 54.60	Ae	2	2.4	*F*160*W* IR	7	3.1±0.6	1
M 2-47	113.8+00.6	23 32 44.79	+62 03 49.11	R/BR	4	0.1–0.2	*F*606*W*	3	4.7	3
CRL 915	218.9−11.7	06 19 58.21	−10 38 14.71	Ae	4	0.4–0.5	[N II]	7	0.85±0.19	1
Hen 2-5[a]	264.4−12.7	07 47 20.03	−51 15 03.39	R	2	0.3	[O III]	7	5.3	3
Hen 2-47	285.6−02.7	10 23 09.14	−60 32 42.32	Ae	4	0.2–0.4	[N II]	7	5.0±0.9	1
Hen 2-90	305.1+01.4	13 09 36.45	−61 19 35.57	R	5	0.4–0.5	Hα	2	2.8±0.5	1
Hen 2-131	315.1−13.0	15 37 11.18	−71 54 52.85	R	5	0.2–0.4	Hα	5	0.6	3
IC 4406	319.6+15.7	14 22 26.27	−44 09 04.35	Ae	3	1.8–2.0	Hα	0	1.6	2
Hen 2-138	320.1−09.6	15 56 01.69	−66 09 09.23	Ad	3	0.4–0.5	Hα	3	5.0	3
Hen 2-142[a]	327.1−02.2	15 59 57.60	−55 55 32.89	Ea	2	0.7	Hα	7	3.4	3
NGC 5882	327.8+10.0	15 16 49.93	−45 38 58.44	BR	2	1.3	[O III]	7	1.67	3
GLMP 531[a]	354.6+04.7	17 13 51.79	−30 49 40.70	R	4	0.3–0.5	*F*606*W*	3	7.0±1.0	1
PM 1-176	356.5−02.3	17 47 22.72	−33 11 09.31	BR	4	0.1–0.3	*F*606*W*	7	5.9±1.2	1

Note. [a]Tentative detections.
References: (1) Vickers et al. (2015), (2) Sabbadin (1984), (3) Cahn, Kaler & Stanghellini (1992).

Table 3. *SST* objects with new rings detection.

Object	PNG	RA (J2000)	Dec. (J2000)	Type	No. of rings	Spacing (arcsec)	Filter	sda shift (pix)	*d* (kpc)	Ref.
NGC 6572	034.6+11.8	18 12 06.36	+06 51 13.01	BR	5	6.0–8.0	8 μm	7	2.54±0.48	1
NGC 7027	084.9−03.4	21 07 01.59	+42 14 10.18	R	6	5.0–8.0	8 μm	5	0.95±0.15	1
Mz 3[a]	331.7−01.0	16 17 13.39	−51 59 10.03	Ad	4	7.0–10.0	8 μm	7	2.20±0.38	1
NGC 6153[a]	341.8+05.4	16 31 30.62	−40 15 12.31	R	3	4.0–5.0	8 μm	5	1.28	2

Note. [a]Tentative detections.
References: (1) Vickers et al. (2015), (2) Cahn et al. (1992).

Table 4. NOT object with new rings detection.

Object	PNG	RA (J2000)	Dec. (J2000)	Type	No. of rings	Spacing (arcsec)	Filter	sda shift (pix)	*d* (kpc)	Ref.
IC 3568	123.6+34.5	12 33 06.87	+82 33 48.95	R	4	3.0-4.0	[O III]	11	2.71	1

References: (1) Cahn et al. (1992).

3.2 Ring-like features: physical or instrumental?

Balick et al. (2001) thoroughly discussed several arguments supporting the authenticity of the ring-like features in NGC 6543, i.e. they are not artefacts of the telescope PSF. In particular, diffraction rings can be expected around bright sources. The brightness spatial profiles of *HST* WFPC2 and WFC3 images of stars with peak intensities similar to those of the brightest sources in our sample showing ring-like structures have been examined, but none of them showed these outer structures. Then, we have examined the brightness spatial profiles of much brighter stars which indeed show diffraction rings, as well as TINYTIM PSF modelling simulations of point-like sources (Krist, Hook & Stoehr 2011). We illustrate our analysis with the *HST* WFPC2 images of the star Prox Cen (Prop. ID 6310, PI: William Fastie).

First, we note that the diffraction rings detected in the images of Prox Cen and TINYTIM simulations are perfectly circular and centred at the location of the star, whereas the rings and arcs detected around PNe are not completely symmetric in most cases, with slightly irregular morphologies. Certainly, the arcs of some sources, such as GLMP 1058 (Appendix Fig. A7), Hen 2-142 (Appendix Fig. A18) and IC 5117 (Appendix Fig. A6), are not circular in shape.

The spatial profile of an *F*814*W* image of Prox Cen is shown in Fig. 5-top, where the position of the diffraction rings is revealed after subtracting an exponential synthetic profile (Fig. 5-middle). The positions and spacing of these rings are consistent with those

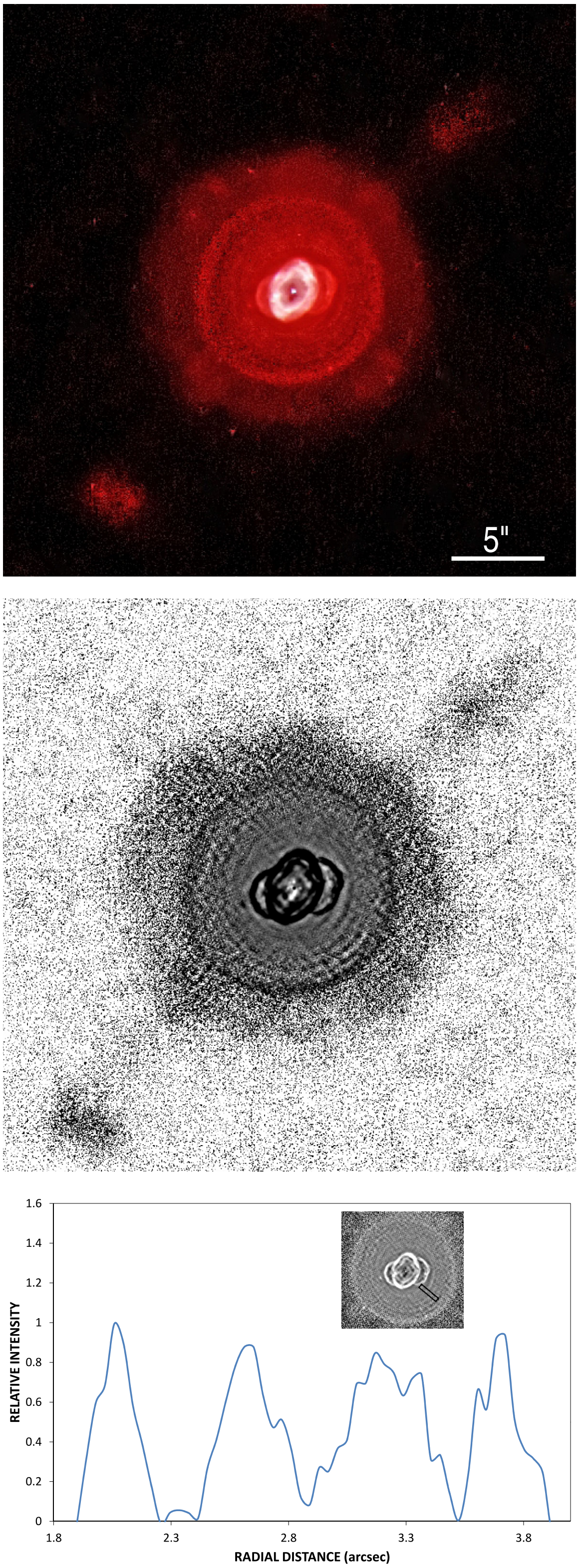

Figure 1. (Top) *HST* colour composite picture of a PN with prototypical type R rings, Vy 1-2, including [O III] (red), *F*200*LP* (green), and *F*350*LP* (blue) unsharp images. (Middle) *HST* [O III]sda image. (Bottom) Profile through the halo ring-like structures derived from the [O III] sda image. The spatial location of the profile is shown in the inset. The underlying emission in this profile has been removed using a least-squares linear fit.

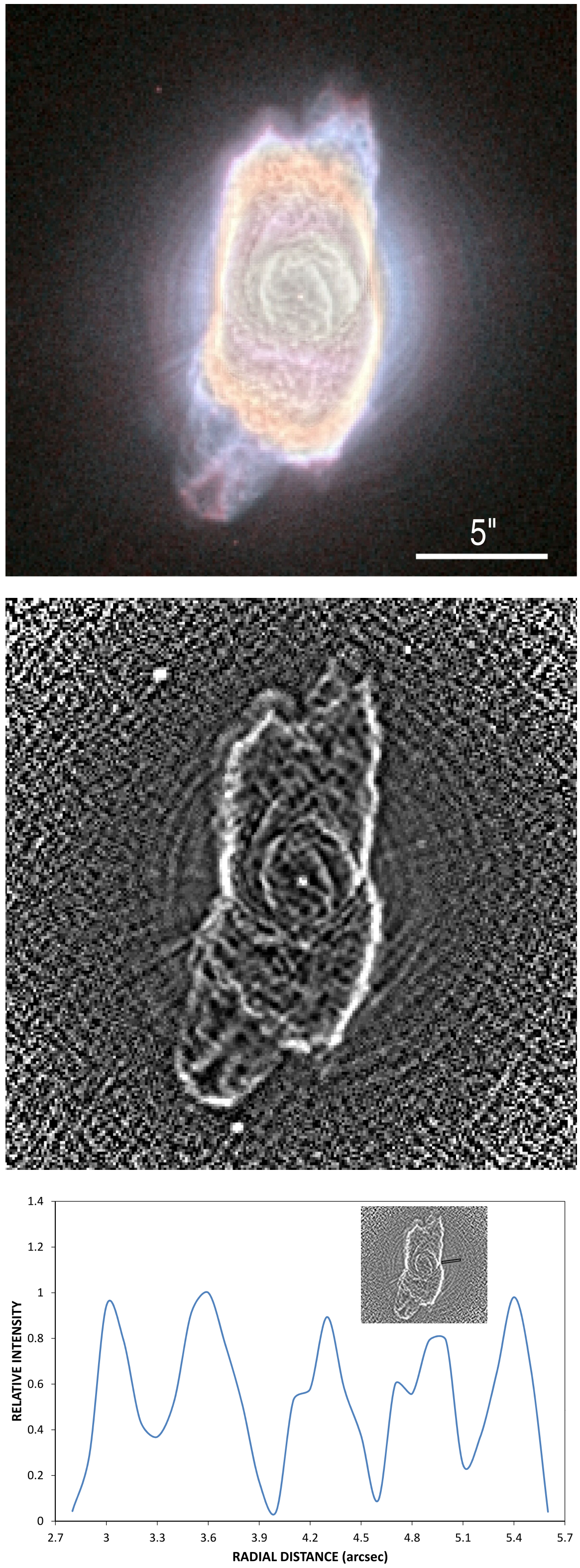

Figure 2. Same as Fig. 1 for NGC 6572, a PN with type BR rings. The *HST* colour composite unsharp picture (top) includes the Hα (red) and [O III] (green-blue) narrow-band images. The sda image (middle) and profile (bottom) correspond to the *HST* [O III] image.

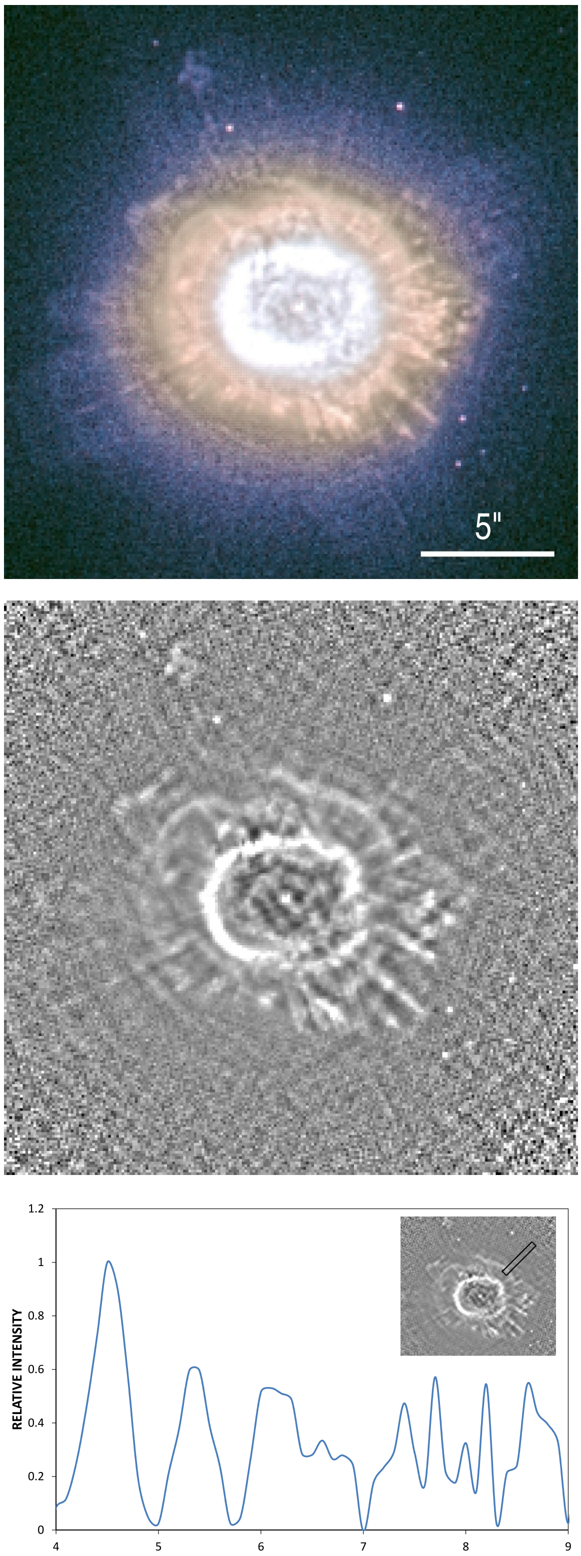

Figure 3. Same as Fig. 1 for BD+30°3639, a PN with R/BR rings. The *HST* colour composite unsharp picture (top) includes the [N II] (red) and Hα (green-blue) narrow-band images. The sda image (middle) and profile (bottom) correspond to the *HST* Hα image.

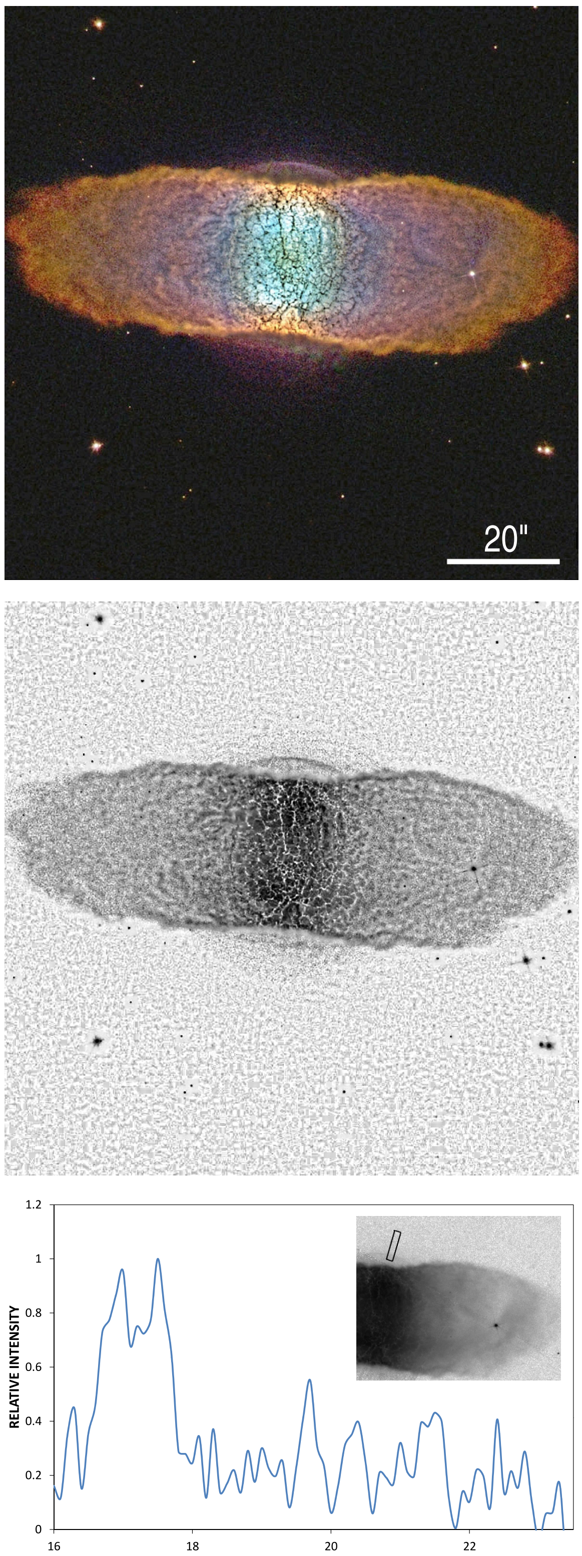

Figure 4. Same as Fig. 1 for IC 4406, a PN with Ae rings. The *HST* colour composite unsharp picture (top) includes the [N II] (red) and Hα (green), and [O III] (blue) narrow-band images. The sda image (middle) and profile (bottom) correspond to the *HST* Hα image.

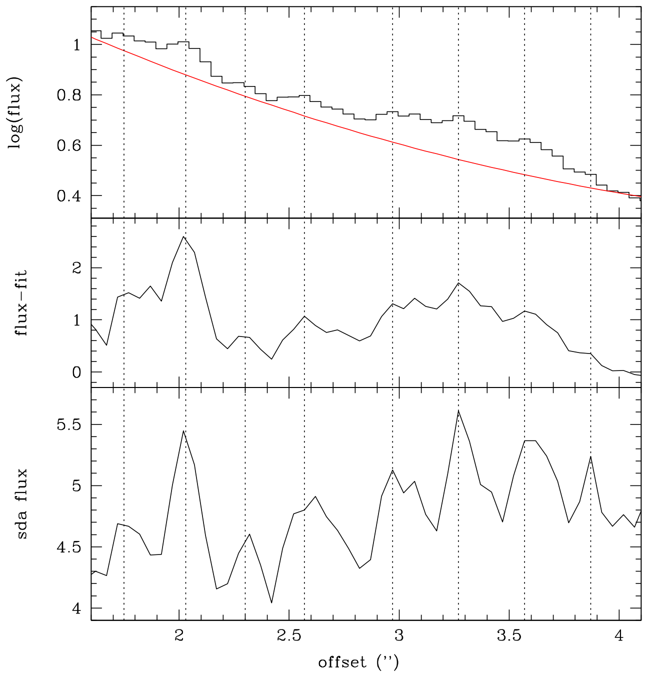

Figure 5. (Top) Spatial profile of Prox Cen extracted from an *HST* WFPC2 image in the *F*814*W* filter. The logarithmic profile can be fitted by a quadratic function (red line) and the residuals of this fit reveal the diffraction rings (middle) as marked by the vertical dotted lines. These are also revealed on the spatial profile of the sda image (bottom).

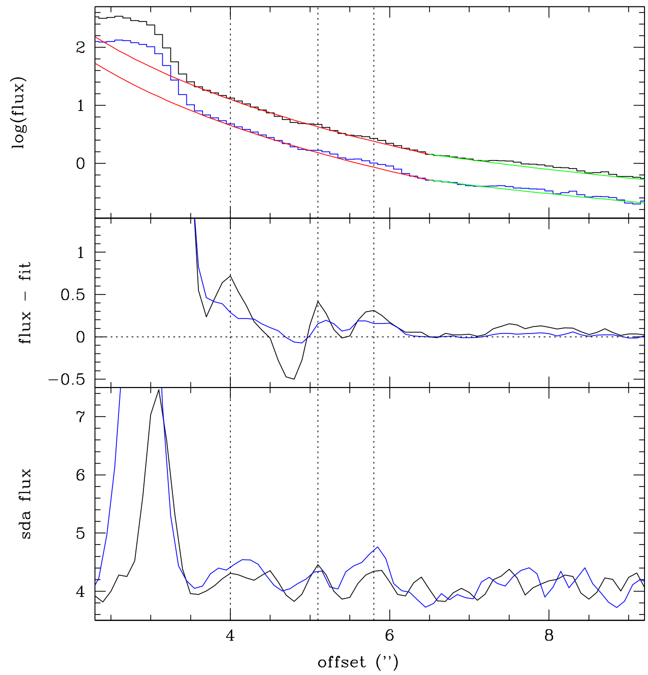

Figure 6. Same as previous figure for the spatial profiles of NGC 6572 extracted from *HST* WFPC2 images in the [O III] (black) and Hα (blue) emission lines. The Hα profile has been shifted by –0.5 dex to allow an easy comparison. The logarithmic profiles of the envelope (red) and halo (green) have been fitted using independent quadratic functions. Both the residuals of these fits (middle) and the sda profiles reveal enhancements in the spatial profiles which are consistent in their location and spacing.

derived after applying the sda method (Fig. 5-bottom). We note here that the spacing between diffraction rings, as determined from the analysis of *F*814*W* images of several bright stars, is always consistent with ∼0.30 arcsec. Similar analysis on an *F*675*W* image of Prox Cen implies diffraction ring spacings ∼0.25 arcsec, i.e. they scale linearly with wavelength as predicted for the radial dimensions of all PSF features. These numbers are consistent with TINYTIM simulations of point sources. On the other hand, the sizes and spacings of the ring-like structures and arcs detected in PNe and proto-PNe do not scale with wavelength, i.e. the wavelength dependence of PSF features is not followed by these structures. This is illustrated in Fig. 6 where the location of these rings are shown for the [O III] and Hα images of NGC 6572. Furthermore, the spacing between ring-like structures of different PNe, as listed in Table 2, vary between 0.1 and 2.0 arcsec.

There is still the possibility that the convolution between diffraction rings and a small (but extended), bright source would produce ring-like structures with separations depending on the source size. This does not seem to be the case. First, the morphology of the ring-like features and arcs is mostly circular, while that of the central nebulae may differ greatly from a round morphology. Secondly, there is not a clear correlation between nebular size and ring spacing; for instance, the central regions of NGC 6572 (Fig. 2) and GLMP 1058 (Appendix Fig. A7) have angular sizes of 5.5 and 1.5 arcsec, respectively, but the ring spacing is very similar in both cases, ∼0.6 and ∼0.5 arcsec, respectively. Then, some sources show these ring-like features at certain emission line filters (e.g. Vy 1-2 shows them in the [O III] emission line registered by the *F*502*N* filter in Fig. 1, but not in the *F*814*W* filter, in spite of the emission being brighter in the latter filter). To double check this last issue, we have examined *HST* WFC3 images in the same filter of two PNe with similar surface brightness, one showing ring-like structures (Vy 1-2) and the other without (Hen 2-203). The spatial brightness profiles of the two PNe are shown in Fig. 7. The ring-like features are clearly detected in the spatial profiles of the direct images of Vy 1-2, and then these are enhanced in the spatial profile of the sda images. On the contrary, no ring-like features are detected in Hen 2-203, and then the sda image does not recover any spurious feature suggesting the presence of ring-like structures. Such results similarly apply to the sample of sources with ring-like features presented in Tables 2–4.

To conclude, the analysis carried out in this section strengthens the idea that the ring-like features detected in the sources listed in Tables 2–4 are not PSF artefacts, but they are true structures in their nebular envelopes. In a few cases, however, these detections are doubtful. Those have been marked as tentative in Tables 2 and 3.

4 RESULTS

The analysis described in the previous section has been carried out on a sample of 655 PNe and proto-PNe with available *HST* and *SST* images. Ground-based NOT observations have been only used for IC 3568. The close inspection of these optical and IR images to search for arcs and ring-like features in the regions just outside the nebular shell has unveiled their presence in 29 PNe. The new PNe showing these features are listed in Tables 2–4. Images and spatial profiles are shown in Figs 1–4 and A1–A25 in the Appendix.

The new discovered low-surface-brightness concentric structures have different extents, from small arcs to almost complete rings. Their relationship with their bright inner shells might also be different. Extending the basic classification of these features into rings and arcs introduced by Corradi et al. (2004), we have classified them into six different types of structures depending on their extent and

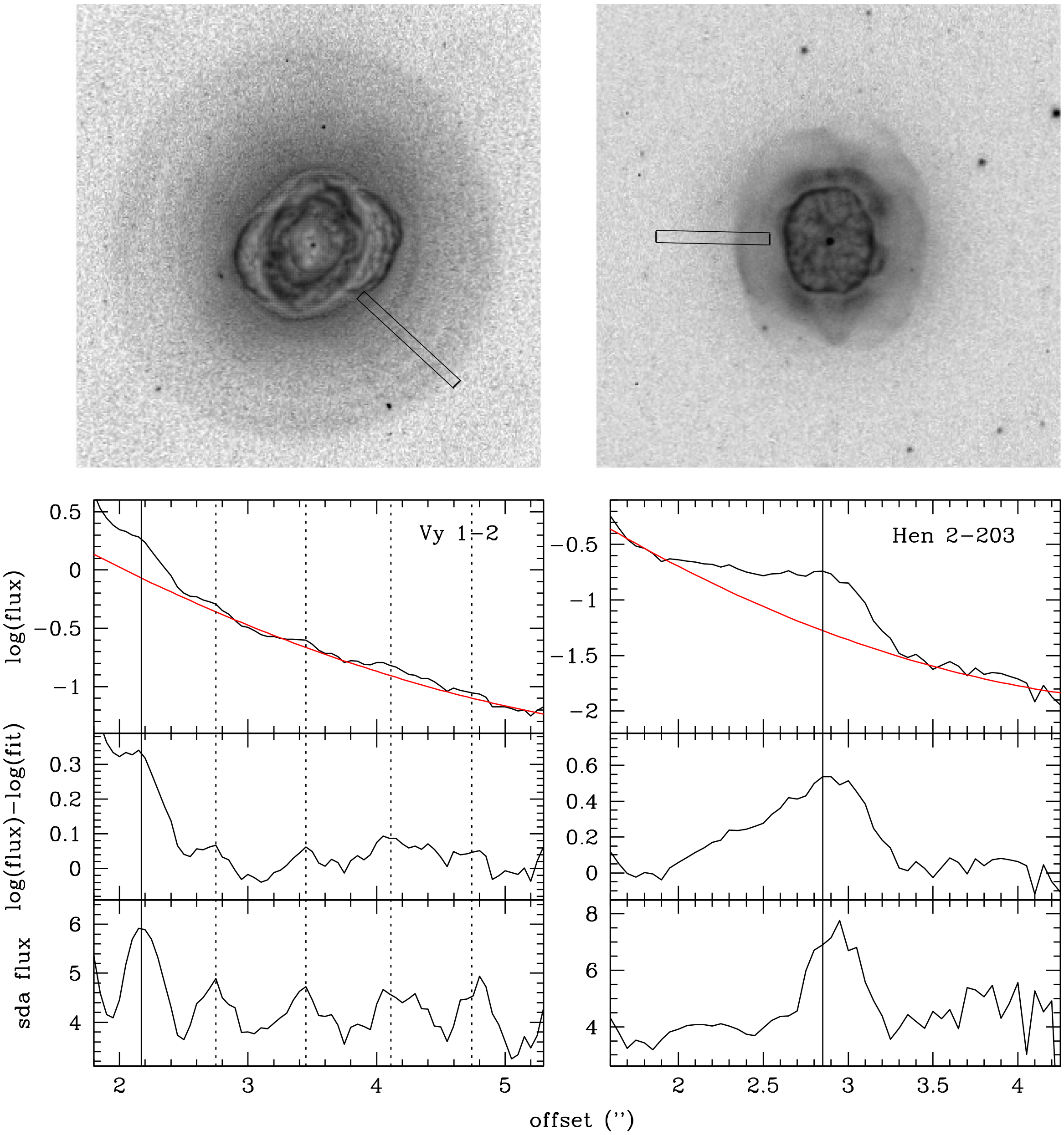

Figure 7. (Top panel) *HST* WFC3 images of Vy 1-2 (left) and Hen 2-203 (right). Spatial profiles have been extracted along the apertures overplotted on these images. (Bottom panel) Spatial profiles (top), residuals of a quadratic fit (middle), and sda (bottom) profiles of Vy 1-2 (left) and Hen 2-203 (right). The location of the inner nebula is marked by a vertical solid line, whereas those of outer ring-like structures in Vy 1-2 are marked by vertical dashed lines.

relationship with the nebular morphology. Basically, in this work we use the term 'ring' for a complete (or mostly complete) round structure and 'arc' for a small round segment. Further details are described in the next section. The morphology of these features for the sources in our sample has been classified in Tables 2–4 following the scheme proposed below.

4.1 Types of outer structures

4.1.1 R: rings

The objects in this category present arcs that can be traced to follow complete (or almost complete) shell-like round structures surrounding a bright inner shell. We will refer to these as rings. The inner shell might have a morphology different from round, but the rings are seen as concentric structures around it. One of the most archetypical R-type object is Vy 1-2 (Fig. 1-top). Besides the two outer bipolar blobs, there is a series of rings between the weak outer halo and the bright inner shell, a high-excitation ring-shaped nebula with two prominent lobes closely resembling NGC 6309 (Vázquez et al. 2008; Rubio et al. 2015)

The sda image (Fig. 1-middle) reveals an appreciable degree of circularity for the rings. If we look carefully, however, we note that the right lobe is probably interacting with one of the inner rings. The distinctive pattern of interwound features is highlighted in the radial profile across the halo shown in the bottom panel of Fig. 1 (see inset for the precise spatial location of the profile). The thickness and distance between these rings seem to be rather uniform, 0.5–0.6 arcsec.

4.1.2 BR: broken rings

The arcs do not trace complete round structures because they are partially intercepted and disrupted by elongated inner shells. This category is illustrated by NGC 6572 (Fig. 2). This PN shows a bright irregular-elliptical inner shell surrounded by a highly asymmetric envelope that has been attributed to the expansion of collimated outflows (Miranda et al. 1999). In the unsharp masking and sda images (Fig. 2-top and middle), this envelope disrupts the rings, producing arcs. It is interesting to note that the arcs actually can be traced through the bipolar outflow. Since the inner shell is tilted by $\simeq 40^\circ$ with respect to the plane of the sky (Masson 1989; Miranda et al. 1999), it can be envisaged that the bipolar outflow has disrupted the rings above and below the plane of the sky.

4.1.3 R–BR: rings/broken rings

There are a few objects whose arcs extents cannot confidentially assign them to either the R or BR types, i.e. it is unclear whether the arcs are complete rings or not. In most cases, this is due to a complex morphology of the inner shell. We have selected the bright source BD+30°3639 (Fig. 3) to illustrate this morphology. The multiple radial filaments and complex morphology of the inner shell revealed in the unsharp masking and sda images do not allow us to conclude whether the outer features are complete ring-like structures or disconnected arcs.

4.1.4 Ae: equatorial arcs

There is a number of highly asymmetric bipolar or multipolar sources that display small arcs enveloping the equatorial waist. The arcs are blocked by the bipolar lobes, thus being constrained above and below the equatorial line. For these features, we have selected the bipolar PN IC 4406 (Fig. 4). This is an extended bipolar PN whose equatorial waist is only slightly less extended than the bipolar lobes. The unsharp image and sda images show a clear arc and hints of two additional outer arcs. The innermost arc is also clearly revealed in the sda surface brightness profile (Fig. 4-bottom).

4.1.5 Ad: disconnected arcs

There is one source, namely Hen 2-138, that displays disconnected sets of arcs along different directions (Appendix Fig. A17). Several arcs are seen along selected directions in the unsharp masking and sda images of this nebula. Apparently, the different blisters of the inner shell may give rise to the morphology of the outer structures as disconnected arcs along selected directions.

4.1.6 Ea: elliptical arcs

Contrary to all sources described above, whose outer rings and arcs are round regardless of the morphology of the inner bright shell, there are two sources, Hen 2-142 (Appendix Fig. A18) and IC 5117 (Appendix Fig. A6) that show arcs with elliptical morphology following that of the bright inner shells.

4.2 Spacing and time lapse between rings and arcs

An inspection of the images and radial profiles of all the sources listed in Tables 2–4 presented in Figs 1–4 and A1–A25 of the Appendix allows us to estimate the number of concentric features and

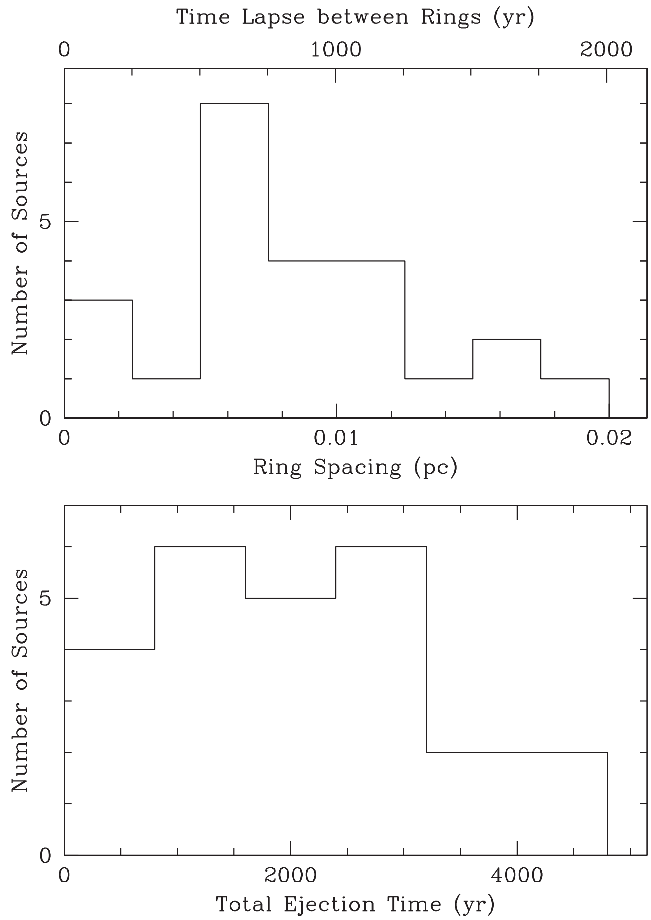

Figure 8. Linear spacing and time lapse between concentric features (top) and total time ejection (bottom) distributions for the objects with ring-like features and arcs detected in *HST* images.

average spacing ($\overline{\Delta\theta}$) between them for each object. The spacing between features ($\Delta\theta$) would depend on their expansion velocity ($v_{\rm exp}$), distance (d), and ejection time lapse between rings ($\Delta\tau$). The information on their distances and averaged spacing listed in Tables 2–4 has been used to derive their typical physical spacing (Δr). The distribution of the physical spacing is shown in Fig. 8-top. The spacing distribution peaks at $\simeq$0.006 pc, with values ranging between 0.0009 pc (Hen 2-131, Appendix Fig. A16) and 0.018 pc. These values are notably smaller than the ring spacing described by Corradi et al. (2004) for evolved PNe, but very similar to those reported by Su (2004) for proto-PNe.

The expansion velocity of rings and arcs in PNe is basically unknown, although they show significant line broadening (Balick et al. 2001). Assuming a typical expansion velocity of 10 km s^{-1} for the AGB envelope, the time lapse between arcs and rings can be estimated from its linear size. The time-lapse distribution is shown in Fig. 8-top. Since the same expansion velocity has been assumed for all sources, this distribution is the same as that of the spacing shown in the same plot. The shortest time lapse is found to be as low as $\simeq$90 yr (Hen 2-131, Appendix Fig. A16). The number of concentric features detected in the sources listed in Tables 2,–4 ranges from two up to six, with an average number of 3.6±1.2. If we account for the number of features, then the total ejection time can also be derived. Its distribution is shown in Fig. 8-bottom. Most

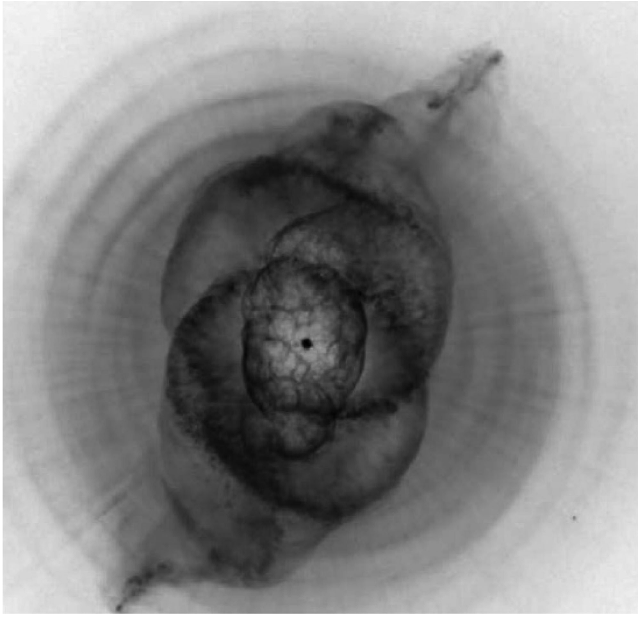

Figure 9. Detailed *HST* [O III]+[N II] ACS image of NGC 6543 (STScI-PRC2004-27) (Corradi 2006). Radial filaments or rays emanating from the main nebula are clearly visible.

objects have total ejection times in the range between 1000 and 3000 yr, with Vy 2-2 (Fig. A3) showing the longest total ejection time ∼4500 yr. Note, however, that the number of ring-like features and arcs and its average should be taken as lower limits, as the outermost features may have fainted below detection limit.

Finally, it is worthwhile to note that the inspection of the spatial profiles of sources showing at least three rings or arcs indicates that the spacing between them does not change dramatically. The relatively constant spacing in a particular object implies that the time lapse between ejections is very stable. This suggests periodic enhancements in the density and/or velocity in the final gasps of the AGB wind. Otherwise, the dynamical effects over these features produced by ionization, by gaseous pressure, or by dust segregation are either negligible or they cause a constant spacing in each source.

4.3 Radial filaments and blisters

Some of the *HST* and *SST* images show a series of radial filaments or rays emanating from the main brightest core. These features are best exemplified in the *HST* picture of NGC 6543 shown in Fig. 9. In some extent, clear examples of our candidates with similar structures are those of NGC 6572 (Fig. 2), M 2-47 (Appendix Fig. A10), and GLMP 1058 (Appendix Fig. A7). The filaments are mostly radial, pointing towards the location of the central star. In general, their surface brightness is small, ≤2 per cent compared to the surface brightness of the main nebula. With variable sizes, they extend sometimes up to 2.7 arcsec.

The systems of radial features or rays are common in many other extended PNe. These radial filaments or rays (nomenclature of Balick 2004) have been described also in NGC 6853 (Hora et al. 2006) and NGC 6543 (Balick 2004), or even in the mid-IR in *SST* observations of NGC 40 (Ramos-Larios, Phillips & Cuesta 2011). The origin of these filaments can be interpreted like 'shadow instabilities' produced by lumps of material or knots and the posterior ionization by the escaping of UV photons (Williams 1999; Balick 2004). Indeed, there is generally a correlation between the detection of a radial shadow and a bright, compact knot at the nebular shell along the line connecting the radial streak with the central star. The latter is clearly shown in the *HST* ratio ([O III]/Hα) images of NGC 3918, NGC 6543, NGC 6720 (Guerrero et al. 2013) or even in a single [N II] sda-processed image of IC 418 (Ramos-Larios et al. 2012) to name a few.

Detailed radiation-hydrodynamic simulations, as those presented by Toalá & Arthur (2014), show that instabilities in the wind–wind interaction zone produce clumps that lead to variations in the opacity. These result in rays of alternating ionized and neutral material.

Moreover, some 'bubble-like' features or blisters observed in the exterior walls of many PNe may imply that the ionized shells of these objects are subject of turbulence and instabilities. These are also detected in the kinematics of the shells (Guerrero, Manchado & Chu 1997).

5 DISCUSSION

5.1 Outer rings and arcs detection rate

In narrow-band optical and mid-IR images from space telescopes, we have searched for weak emission features around the bright inner shells of PNe and proto-PNe. The detailed analysis of these observations has revealed for the first time different faint structures outside the main nebular shell, including radial rays and blisters, but here we focus on the presence of ring-like features and arcs. A growing number of rings and arcs around nebular shells of PNe and proto-PNe have been reported in recent years (e.g. Corradi et al. 2004; Kwok & Su 2005; Ramos-Larios, Phillips & Cuesta 2011; Sahai, Morris & Villar 2011). The list of sources with rings and arcs compiled from these works are summarized in Table 5. The new detections reported in this work in Tables 2–4 doubles the number of PNe and proto-PNe with known rings and arcs surrounding their bright nebular shells, from 29 up to 58.

In accordance with previous results (e.g. Corradi et al. 2004), we find that ring-like features and arcs can be found among different morphological types, although there is a tendency in our sample to find them around sources with bipolar or multipolar morphologies (∼64 per cent) with respect to those with elliptical morphology (∼29 per cent). Otherwise, rings and arcs are scarce among sources with round morphologies (∼7 per cent).

It has been suggested that the spacing between these outer structures increases with time (Corradi et al. 2004). The spacing between rings and arcs of the objects in our sample are generally smaller than those reported by Corradi et al. (2004). The small size of the objects in our sample (see Figs 1–4 and A1–A25) suggests that they are young, thus reinforcing the conclusion that the spacing between rings and arcs increases with time. If this is the case, then our sample is probing values of the time lapse closer to their true values, before the spacing between concentric features widens.

Our investigation has detected ring-like features and arcs in 29 new PNe and proto-PNe from a sample of ∼655 sources. Adding those to the 29 previous detections in Table 5 and accounting for the non-detections reported in original references, we derive a detection rate ≃8 per cent over a sample in excess of 700 sources. This detection rate is notably smaller than that previously derived by Corradi et al. (2004, 35 per cent), who suggested that these features might be present in nearly all PNe, provided the observations are sufficiently sensitive. Contrary to this suggestion, we have not

Table 5. Optical (*HST*) and IR (*Spitzer*) objects with reported rings detection.

Object	PNG	RA (J2000)	Dec. (J2000)	Common name	Detection band	References
CRL 5385	004.2+02.1	17 47 13.49	−24 12 51.42	Silkworm	Opt	1
HD 179821	035.6−04.9	19 13 58.60	+00 07 31.93		Opt	2
NGC 7009	037.7−34.5	21 04 10.87	−11 21 48.26	Saturn	Opt	3
NGC 6853	060.8−03.6	19 59 36.37	+22 43 15.75	Dumbbell	Opt/IR	4
NGC 6881	074.5+02.1	20 10 52.45	+37 24 42.40		Opt	3
GLMP 968	075.4+04.1	20 04 35.98	+39 18 44.50		Opt	5
CRL 2688	080.1−06.5	21 02 18.27	+36 41 37.01	Egg	Opt	6
NGC 7027	084.9−03.4	21 07 01.59	+42 14 10.18		Opt	2,7
NGC 7026	089.0+00.3	21 06 18.23	+47 51 07.15		Opt	3
CRL 3068	093.5−40.3	23 19 12.60	+17 11 33.13		Opt	8
NGC 6543	096.4+29.9	17 58 33.42	+66 37 59.52	Cat's Eye	Opt	9
NGC 7662	106.5−17.6	23 25 53.61	+42 32 06.02	Snowball	Opt	3
NGC 7354	107.8+02.3	22 40 19.83	+61 17 08.72		IR	10
NGC 40	120.0+09.8	00 13 01.01	+72 31 19.09		Opt/IR	3,11
IRC+10011	128.6−50.1	01 06 25.98	+12 35 53.01		Opt	8
CRL 618	166.4−06.5	04 42 53.64	+36 06 53.42		Opt	12
IRC+30219	197.7+55.9	10 16 02.27	+30 34 18.61	CIT 6	Opt	13
NGC 1535	206.4−40.5	04 14 15.78	−12 44 21.68		Opt	3
NGC 2346	215.6+03.6	07 09 22.52	−00 48 23.62		IR	14
IRC+10216	221.4+45.0	09 47 57.40	+13 16 43.56	Peanut	Opt	15
IRC-30015	250.1−80.5	01 26 58.09	−32 32 35.44	R Sculptoris	Opt	16
NGC 3242	261.0+32.0	10 24 46.10	−18 38 32.64	Jupiter's Ghost	Opt/IR	3,10
Roberts 22	284.1−00.7	10 21 33.82	−58 05 48.26		Opt	17
IC 2448	285.7−14.9	09 07 06.26	−69 56 30.57		Opt	3
NGC 3918	294.6+04.7	11 50 17.73	−57 10 56.90		Opt	18
GLMP 507	340.3−03.2	17 03 10.08	−47 00 27.70	Water Lily	Opt	5
CGCS 3748	343.5+00.3	16 58 06.27	−42 19 23.91	IRAS 16545−4214	Opt	19
CRL 6815	353.8+02.9	17 18 19.85	−32 27 21.63	Cotton Candy	Opt	20
Hb 5	359.3−00.9	17 47 56.18	−29 59 41.91		Opt	2,7

References: (1) Su et al. (1998), (2) Su (2004), (3) Corradi et al. (2004), (4) Kwok et al. (2008), (5) Hrivnak et al. (2001), (6) Sahai et al. (1998), (7) Terzian & Hajian (2000), (8) Mauron & Huggins (2006), (9) Balick et al. (2001), (10) Phillips et al. (2009), (11) Ramos-Larios et al. (2011), (12) Balick et al. (2013), (13) Dinh-V.-Trung & Lim (2009), (14) Phillips & Ramos-Larios (2010), (15) Mauron & Huggins (1999), (16) Maercker et al. (2012), (17) Sahai et al. (1999), (18) Corradi et al. (2003), (19) Balick et al., 'The Catalog of Hubble Images of Nascent and Infantile Planetary Nebulae', (20) Kwok et al. (1998).

detected rings or arcs in a considerable number of proto-PNe and PNe with *HST* observations as deep (or even deeper) than those of sources with detected rings or arcs. It is thus questionable that rings and/or arcs outside the bright nebular shells of proto-PNe and PNe are ubiquitous. It can be argued that these features are only produced at certain phases of the TPs or under very specific conditions (evolution through a common-envelope phase, presence of magnetic fields, effects of a binary companion or planetary system), or that they fade away quickly and have short lifetimes. Different possibilities are discussed below.

5.2 Origin of rings and arcs

The observational history of this phenomenon is short and thus there is little information on the physical and kinematical properties of rings and arcs around the main nebular shells of PNe and proto-PNe. The most accepted scenario implies that they are associated to (quasi-) periodic enhancements in the mass-loss rate at the final stages of the AGB evolution. Several hypotheses have been suggested to explain the underlying causes of these variations, but no consensus on single or main mechanism has been reached. The study of the characteristics of the morphology, spatial distribution and spacing of the rings and arcs can help us to identify the different processes involved in their formation.

Among all the processes leading to a temporal modulation of the mass-loss, TPs are the first that can be dismissed. Those large amount of mass release are punctual episodes occurring during the AGB phase. The interpulse period is expected to be in the range 10^4–10^5 yr (Vassiliadis & Wood 1993). In general, these interpulse periods are larger than the time lapses $\Delta\tau$ between successive annular features derived in Section 4.2, which are shorter than 2000 yr (Fig. 8, top). This inconsistency between the periodicities and time-scale of rings and arcs and some mechanisms associated to helium shell flashes had been previously noted by Sahai & Trauger (1998) and Kwok et al. (1998).

On the other side of $\Delta\tau$ scale, we can also discard AGB pulsations as the origin for rings and arcs. These stars undergo radial pulsations whose regularity differ depending on the type of objects, i.e. Mira, semiregular and irregular types for the most periodic to totally irregular pulsation pattern, respectively. Overall, the period is about 1–2 yr (see Willson & Marengo 2012), which is much shorter than the shortest $\Delta\tau$ of 90 yr (Hen 2-131). Similarly, other processes in evolved stars such as fuel-supply relaxation oscillations (Van Horn et al. 2003) and variations in the periods of pulsation causes a change in the stellar structure (Zijlstra, Bedding & Mattei

2002) producing only short-term variations in mass-loss. Solar-type cycles in magnetic activity have also been proposed to be capable to generate fluctuations in the mass-loss rate (Soker 2000). García-Segura, López & Franco (2001) point out that solar-like polarity inversions of the progenitor magnetic field may affect a magnetized stellar wind, leading to formation of circularly symmetric features by pressure oscillations. Although the model does not include the dynamic effects of dust grains, strong magnetic fields were able to reproduce the features in the morphology of Hen 2-90. However, it is worth noting that the magnetic cycle in AGB stars is shorter compared to the time lapse between rings and arcs (Meijerink, Mellema & Simis 2003).

Alternatively, the long-period oscillations in the evolved AGB star has been suggested to produce multiperiodicity or chaotic motions (Icke, Frank & Heske 1992), none the less is still uncertain if they are relevant to explain the formation of ring-like features (Soker 2000). A mechanism of a completely different nature, not related to mass-loss enhancements, implies the formation of the density-enhancements by the viscous momentum coupling between outflowing gas and dust (Simis et al. 2001; Meijerink et al. 2003). The expected morphology closely resembles that observed in young PNe. The drift of dust grains respect to the AGB shell produce spherically shapes with enhanced dust-to-gas ratios. However, mid-IR observations show that the dust and gaseous components of rings are in register (e.g. Phillips et al. 2009; Ramos-Larios et al. 2011).

There are cases in which a binary interaction can be invoked in order to explain the observed patterns. Indeed, Mastrodemos & Morris (1999) and more recently Kim & Taam (2012a,b) and Kim et al. (2013) have suggested that the mass-loss from a binary star could have the enough potential to produce spiral shocks or even incomplete ring-like patterns. These will result in density enhancements very similar to rings observed in AGB stars and PNe.

There are at least two types of annular structures that can be associated to specific formation mechanisms. The spiral-like arcs detected mainly in AGB stars such as AFGL 3068 (Mauron & Huggins 2006) or CIT 6 (Dinh-V.-Trung & Lim 2009). They are also very interesting due to the low representation of more evolved objects displaying spiral structures that have been associated to binary systems. The other group whose outer features could be explained by the action of a binary system is the one presenting elliptical arcs (Ea). The periastron passage of a stellar companion proposed by Harpaz, Rappaport & Soker (1997) might modulate in some sense the progenitor mass-loss rates via periodic cessations of the isotropic wind. An eccentric orbit would lead to non-circular rings. Its occurrence rate among PNe is also low.

The identification of the mechanism leading to the formation of the rings and arcs for each object in our sample may require individual investigations. Our results, in conjunction with those presented by Corradi et al. (2004), indicate that the mechanism responsible for the formation of these annular features is 'stable' in time-scales in excess of several thousand years. This mechanism is also relatively regular, with constant inter-ring/arc spacings within each source. Finally, the symmetry of the rings, mostly circular, and their extent, embracing the whole inner nebula (type R) imply that this mechanism produces global, isotropic, spherically symmetric density enhancements in the AGB wind. Even the non-concentric or non-circular features in type BR, R–BR, Ae, and Ad rings and arcs could have been well-defined circular ring-like features in the past, later disrupted by the emergence of new structures such as jets or outflows. Such scenario could explain the rings morphology and distribution in NGC 6543 (Balick et al. 2001).

Otherwise, 'unstable' mechanisms, occurring on irregular time-scales and/or resulting in anisotropic distributions of material, are basically dismissed by the low occurrence of completely disturbed structures in the available sample of sources with ring-like features. Certainly this would not apply if the formation of chaotic structures is followed by a process that promotes their regularization into equally spaced and round features.

There are 20 post-AGB/proto-PNe, and 38 PNe listed in Tables 2–5. These numbers underline the survival of these structures up to the latest phases of stellar evolution, beyond the onset of the fast stellar wind and ionization of the nebula by the increasing stellar UV flux. Note, however, that arcs and rings are seen in both post-AGB stars/proto-PNe and PNe, but spiral structures are only observed in post-AGB stars.

The interaction of these round outer features with the main nebular shells, due to their different expansion velocities and nebular expansion, their fixed spacing in a particular source and their symmetry deserve detailed attention. The formation and evolution with time of density enhancements in the AGB wind require detailed radiation-hydrodynamical simulations. These are presently not available, but we have started a program to carry out these simulations (Toalá et al., in preparation). The extent of these simulations make them beyond the scope of this paper.

6 SUMMARY

We report the first detection of ring-like structures and arcs around the bright nebular shells of 29 PNe and proto-PNe. The sensitivity and excellent imaging capabilities of the *HST* have been critical to detect these features given their small angular size and low surface brightness, although they can be also detected in ground-based optical and space-based mid-IR images. The occurrence rate of rings and arcs in post-AGB stars, proto-PNe, and PNe is low, ~8 per cent. This conclusion, based on the investigation of high-quality images of a sample of >700 sources, is opposite to previous suggestions derived from smaller samples that rings and arcs are ubiquitous.

The high-resolution *HST* images have been used to refine the morphological classification of these features around the main nebular shells of proto-PNe and PNe. We identify complete rings (R), broken-rings (BR), and intermediate cases between these two (R–BR). There are also equatorial arcs (Ae), disconnected arcs (Ad), and elliptical arcs (Ea). We suggest that some of the BR, R–BR, Ae, and Ad proceed from complete rings that have been swept up along some directions by the growing nebular shell.

The radial profile of the external regions of these nebulae have been analysed to investigate the spacing, interfeature time lapse, number of rings and arcs, and total ejection time. This has involved using a technique to subtract the smoother, underlying emission component of the envelope in radial profiles to emphasize the ring-like features and arcs. Typical ring and arc numbers of 3.6±1.2 are found. The time lapse between them is typically in the range 500–1200 yr and the total ejection time is ≤4500 yr in our sample.

We discuss the proposed scenarios for the formation of ring-like structures in the basis of their morphological and statistical properties. Our investigation has increased the number of late evolved stars with detected rings and arcs, but their frequency of occurrence is low. This either indicates that only a small fraction of the progenitor stars produce these structures or that they disappear with the nebular evolution. At any rate, the total time lapse of these structures in time and their periodicity point to formation mechanisms stable in periods of time of a few thousand years. It is difficult at this time to assess which mechanism is operating solely based on imagery.

Our comprehension of this phenomenon is still quite limited. High-resolution observations and detailed radiation-hydrodynamical simulations are needed to have a better understanding of the interaction of the main nebular shells and ionizing photon flux early in the PN phase with the last gasps of mass-loss taking place at the late stages of the AGB phase. These simulations are in progress and will be published as the second paper of this series (Toalá et al., in preparation).

ACKNOWLEDGEMENTS

GRL acknowledges support from CONACyT (grant 177864), CGCI, PROMEP, and SEP (Mexico). ES acknowledges support from CONACyT (grant 22011). LS acknowledges support from UNAM-PAPIIT grant IA101316. MAG also acknowledges support of the grant AYA 2011-29754-C03-02 and AYA 2014-57280-P, both co-funded with FEDER funds.

This research has made use of the NASA/IPAC Infrared Science Archive, which is operated by the Jet Propulsion Laboratory, California Institute of Technology, under contract with the National Aeronautics and Space Administration. Based on observations made with the NASA/ESA *HST*, and obtained from the MAST and Hubble Legacy Archive, which is a collaboration between the Space Telescope Science Institute (STScI/NASA), the Space Telescope European Coordinating Facility (ST-ECF/ESA), and the Canadian Astronomy Data Centre (CADC/NRC/CSA).

REFERENCES

Avila R. et al., 2015, ACS Instrument Handbook, Version 14.0. STScI, Baltimore
Balick B., 2004, AJ, 127, 2262
Balick B., Frank A., 2002, ARA&A, 40, 439
Balick B., Gonzalez G., Frank A., Jacoby G., 1992, ApJ, 392, 582
Balick B., Wilson J., Hajian A. R., 2001, AJ, 121, 354
Balick B., Huarte-Espinosa M., Frank A., Gomez T., Alcolea J., Corradi R. L. M., Vinković D., 2013, ApJ, 772, 20
Cahn J. H., Kaler J. B., Stanghellini L., 1992, A&AS, 94, 399
Chu Y.-H., Jacoby G. H., Arendt R., 1987, ApJS, 64, 529
Corradi R. L. M., 2006, in Barlow M. J., Méndez R. H., eds, Proc. IAU Symp. 234, Planetary Nebulae in our Galaxy and Beyond. Cambridge Univ. Press, Cambridge, p. 277
Corradi R. L. M., Schönberner D., Steffen M., Perinotto M., 2003, MNRAS, 340, 417
Corradi R. L. M., Sánchez-Blázquez P., Mellema G., Giammanco C., Schwarz H. E., 2004, A&A, 417, 637
Dinh-V.-Trung, Lim J., 2009, ApJ, 701, 292
Dressel L., 2015, Wide Field Camera 3 Instrument Handbook, Version 7.0. STScI, Baltimore
Fazio G. G. et al., 2004, ApJS, 154, 10
García-Segura G., López J. A., Franco J., 2001, ApJ, 560, 928
Guerrero M. A., Manchado A., Chu Y.-H., 1997, ApJ, 487, 328
Guerrero M. A., Toalá J. A., Medina J. J., Luridiana V., Miranda L. F., Riera A., Velázquez P. F., 2013, A&A, 557, A121
Hajian A. R., Frank A., Balick B., Terzian Y., 1997, ApJ, 477, 226
Harpaz A., Rappaport S., Soker N., 1997, ApJ, 487, 809
Hora J. L., Latter W. B., Allen L. E., Marengo M., Deutsch L. K., Pipher J. L., 2004, ApJS, 154, 296
Hora J. L., Latter W. B., Smith H. A., Marengo M., 2006, ApJ, 652, 426
Hrivnak B. J., Kwok S., Su K. Y. L., 2001, AJ, 121, 2775
Hyung S., Mellema G., Lee S.-J., Kim H., 2001, A&A, 378, 587
Icke V., Frank A., Heske A., 1992, A&A, 258, 341
Kim H., Taam R. E., 2012a, ApJ, 744, 136
Kim H., Taam R. E., 2012b, ApJ, 759, 59
Kim H., Hsieh I.-T., Liu S.-Y., Taam R. E., 2013, ApJ, 776, 86
Krist J. E., Hook R. N., Stoehr F., 2011, in Kahan M. A., ed., Proc. SPIE Conf. Ser. Vol. 8127, Optical Modeling and Performance Predictions V. SPIE, Bellingham, p. 81270J
Kwok S., 2001, in Szczerba R., Górny S. K., eds, Astrophysics and Space Science Library, Vol. 265, Post-AGB Objects as a Phase of Stellar Evolution. Kluwer, Dordrecht, p. 3
Kwok S., Hsia C. H., 2007, ApJ, 660, 341
Kwok S., Su K. Y. L., 2005, ApJ, 635, L49
Kwok S., Su K. Y. L., Hrivnak B. J., 1998, ApJ, 501, L117
Kwok S., Su K. Y. L., Stoesz J. A., 2001, in Szczerba R., Górny S. K., eds, Astrophysics and Space Science Library, Vol. 265, Post-AGB Objects as a Phase of Stellar Evolution. Kluwer, Dordrecht, p. 115
Kwok S., Chong S.-N., Koning N., Hua T., Yan C.-H., 2008, ApJ, 689, 219
Levi L., 1974, Comput. Graph. Image Process., 3, 163
McMaster B. et al., 2008, WFPC2 Instrument Handbook, Version 10.0. STScI, Baltimore
Maercker M. et al., 2012, Nature, 490, 232
Masson C. R., 1989, ApJ, 336, 294
Mastrodemos N., Morris M., 1999, ApJ, 523, 357
Mauron N., Huggins P. J., 1999, A&A, 349, 203
Mauron N., Huggins P. J., 2006, A&A, 452, 257
Meijerink R., Mellema G., Simis Y., 2003, A&A, 405, 1075
Mellema G., 1994, A&A, 290, 915
Miranda L. F., Vázquez R., Corradi R. L. M., Guerrero M. A., López J. A., Torrelles J. M., 1999, ApJ, 520, 714
Perinotto M., Schönberner D., Steffen M., Calonaci C., 2004, A&A, 414, 993
Phillips J. P., Ramos-Larios G., 2010, MNRAS, 405, 2179
Phillips J. P., Ramos-Larios G., Schröder K.-P., Contreras J. L. V., 2009, MNRAS, 399, 1126
Ramos-Larios G., Phillips J. P., 2008, MNRAS, 390, 1014
Ramos-Larios G., Phillips J. P., Cuesta L. C., 2011, MNRAS, 411, 1245
Ramos-Larios G., Vázquez R., Guerrero M. A., Olguín L., Marquez-Lugo R. A., Bravo-Alfaro H., 2012, MNRAS, 423, 3753
Rubio G., Vázquez R., Ramos-Larios G., Guerrero M. A., Olguín L., Guillén P. F., Mata H., 2015, MNRAS, 446, 1931
Sabbadin F., 1984, A&AS, 58, 273
Sahai R., Trauger J. T., 1998, AJ, 116, 1357
Sahai R. et al., 1998, ApJ, 493, 301
Sahai R., Zijlstra A., Bujarrabal V., te Lintel Hekkert P., 1999, AJ, 117, 1408
Sahai R., Morris M. R., Villar G. G., 2011, AJ, 141, 134
Shchelkanova A. Y., 1987, Sov. Astron. Lett., 13, 120
Simis Y. J. W., Icke V., Dominik C., 2001, A&A, 371, 205
Soker N., 2000, ApJ, 540, 436
Stanghellini L., Pasquali A., 1995, ApJ, 452, 286
Su K. Y. L., 2004, in Meixner M., Kastner J. H., Balick B., Soker N., ASP Conf. Ser. Vol. 313, Asymmetrical Planetary Nebulae III: Winds, Structure and the Thunderbird. Astron. Soc. Pac., San Francisco, p. 247
Su K. Y. L., Volk K., Kwok S., Hrivnak B. J., 1998, ApJ, 508, 744
Terzian Y., Hajian A. R., 2000, in Kastner J. H., Soker N., Rappaport S., eds, ASP Conf. Ser. Vol. 199, Asymmetrical Planetary Nebulae II: From Origins to Microstructures. Astron. Soc. Pac., San Francisco, p. 33
Thatte D., Dahlen T., Barker E., de Jong R., Koekemoer A., Pirzkal N., Viana A., Wiklind T., 2009, NICMOS Data Handbook, Version 8.0. STScI, Baltimore
Toalá J. A., Arthur S. J., 2014, MNRAS, 443, 3486
Van Horn H. M., Thomas J. H., Frank A., Blackman E. G., 2003, ApJ, 585, 983
Vassiliadis E., Wood P. R., 1993, ApJ, 413, 641
Vázquez R., Miranda L. F., Olguín L., Ayala S., Torrelles J. M., Contreras M. E., Guillén P. F., 2008, A&A, 481, 107
Vickers S. B., Frew D. J., Parker Q. A., Bojičić I. S., 2015, MNRAS, 447, 1673
Villaver E., García-Segura G., Manchado A., 2002a, ApJ, 571, 880
Villaver E., Manchado A., García-Segura G., 2002b, ApJ, 581, 1204
Williams R. J. R., 1999, MNRAS, 310, 789
Willson L. A., Marengo M., 2012, J. Am. Assoc. Var. Star Obs., 40, 516
Zijlstra A. A., Bedding T. R., Mattei J. A., 2002, MNRAS, 334, 498

APPENDIX

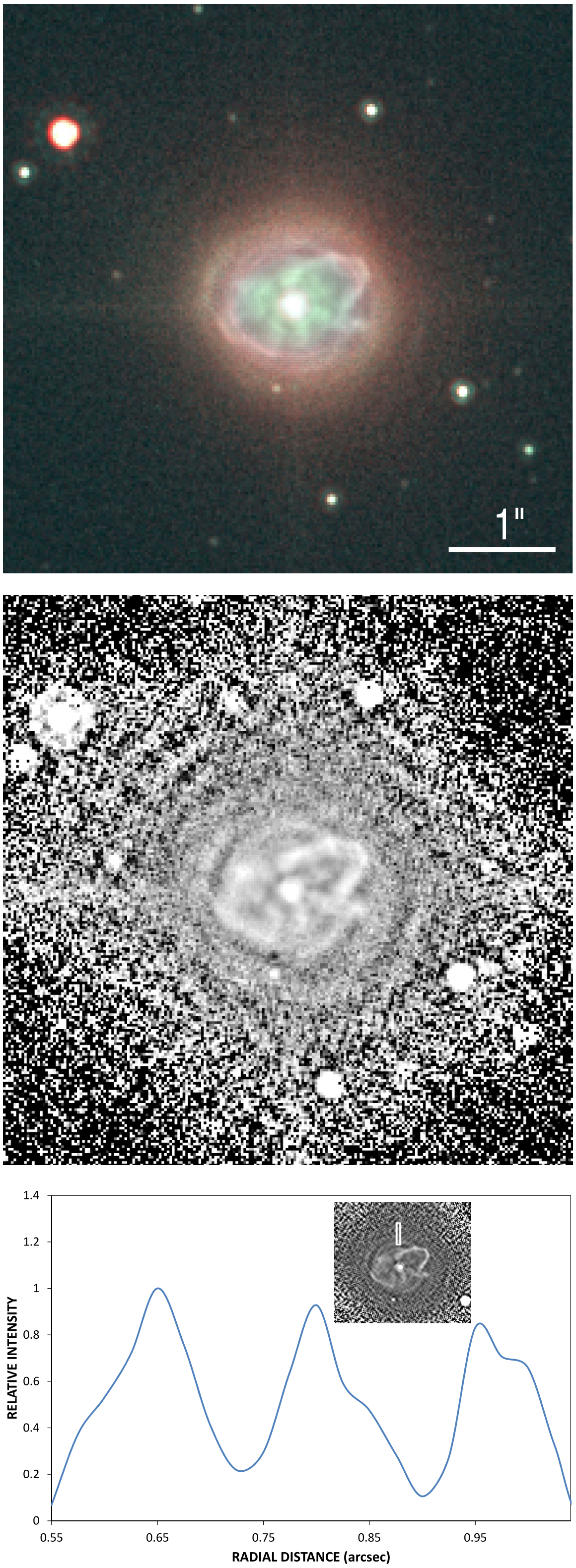

Figure A1. Same as Fig. 1 for PM 1-255. The *HST* colour composite unsharp picture (top) includes the *F*814*W* (red) and *F*606*W* (green-blue) broad-band images. The sda image (middle) and profile (bottom) correspond to the *HST F*606*W* image.

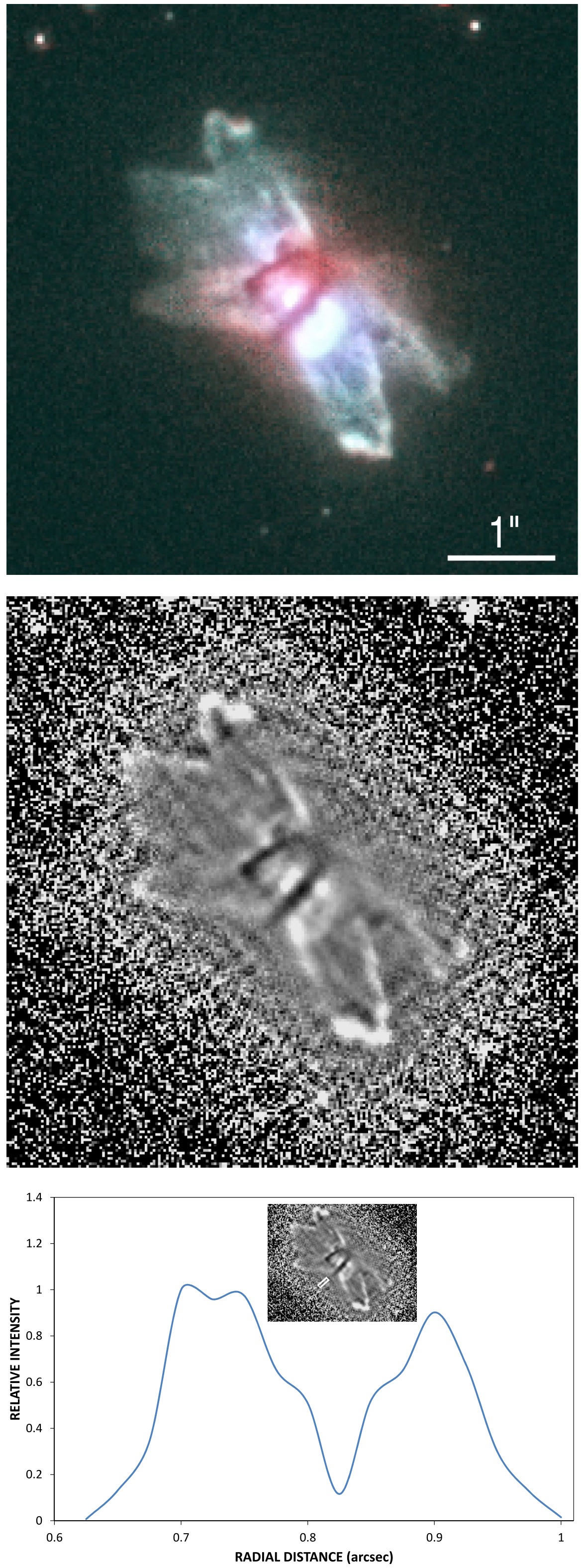

Figure A2. Same as Fig. 1 for GLMP 870. The *HST* colour composite unsharp picture (top) includes the *F*814*W* (red) and *F*606*W* (green-blue) broad-band images. The sda image (middle) and profile (bottom) correspond to the *HST F*606*W* image.

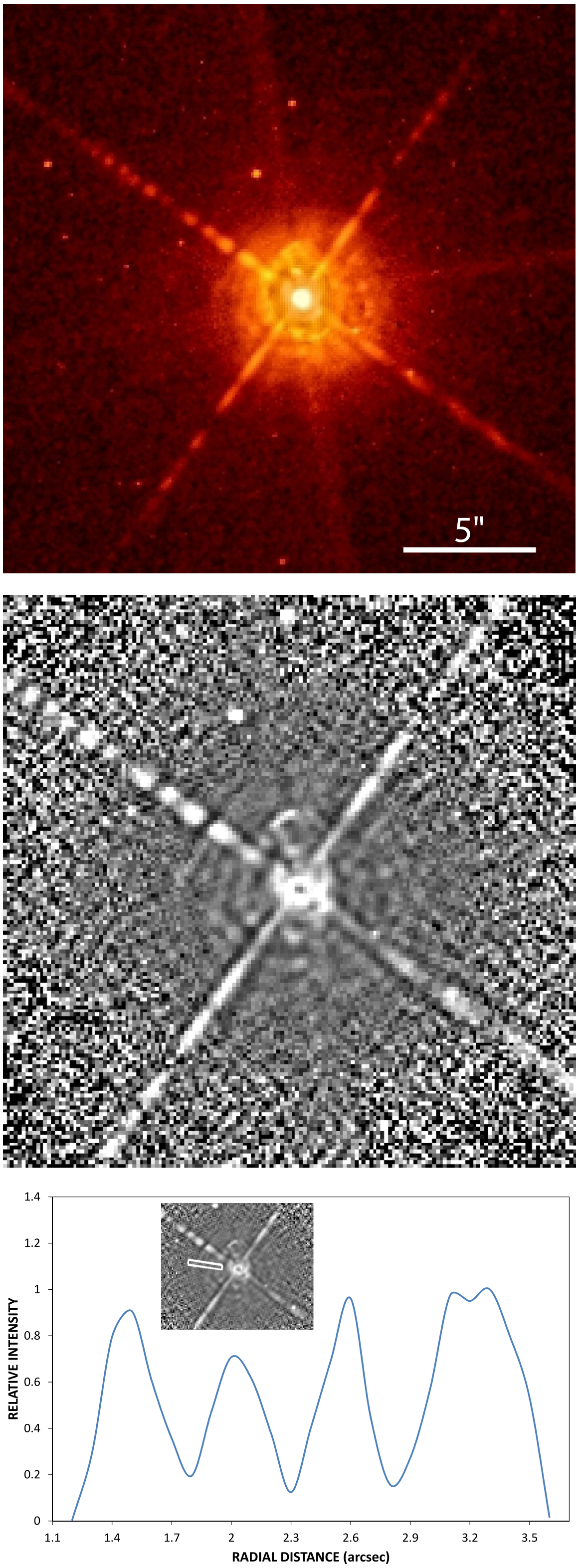

Figure A3. Same as Fig. 1 for Vy 2-2. The *HST* unsharp picture (top) includes only the Hα (red) narrow-band image. The sda image (middle) and profile (bottom) correspond to the *HST* Hα image.

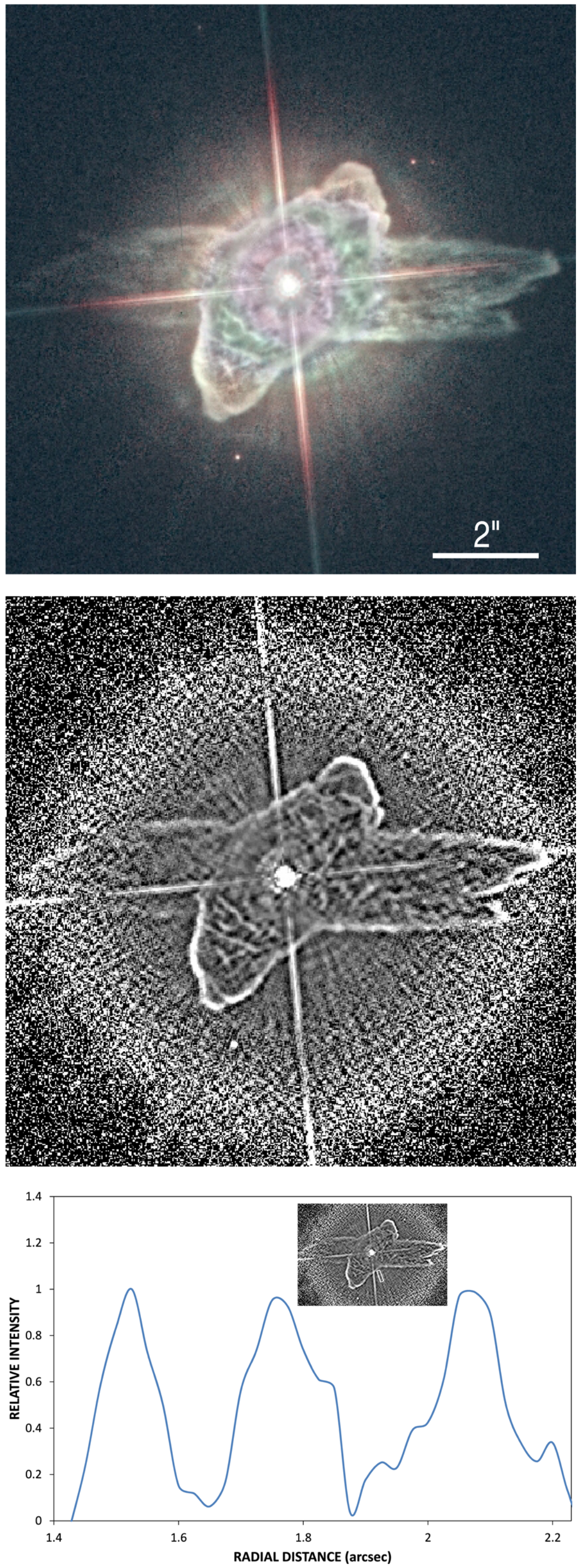

Figure A4. Same as Fig. 1 for PM 2-42. The *HST* colour composite unsharp picture (top) includes the *F*606*W* (red) and *F*435*W* (green-blue) broad-band images. The sda image (middle) and profile (bottom) correspond to the *HST* *F*435*W* image.

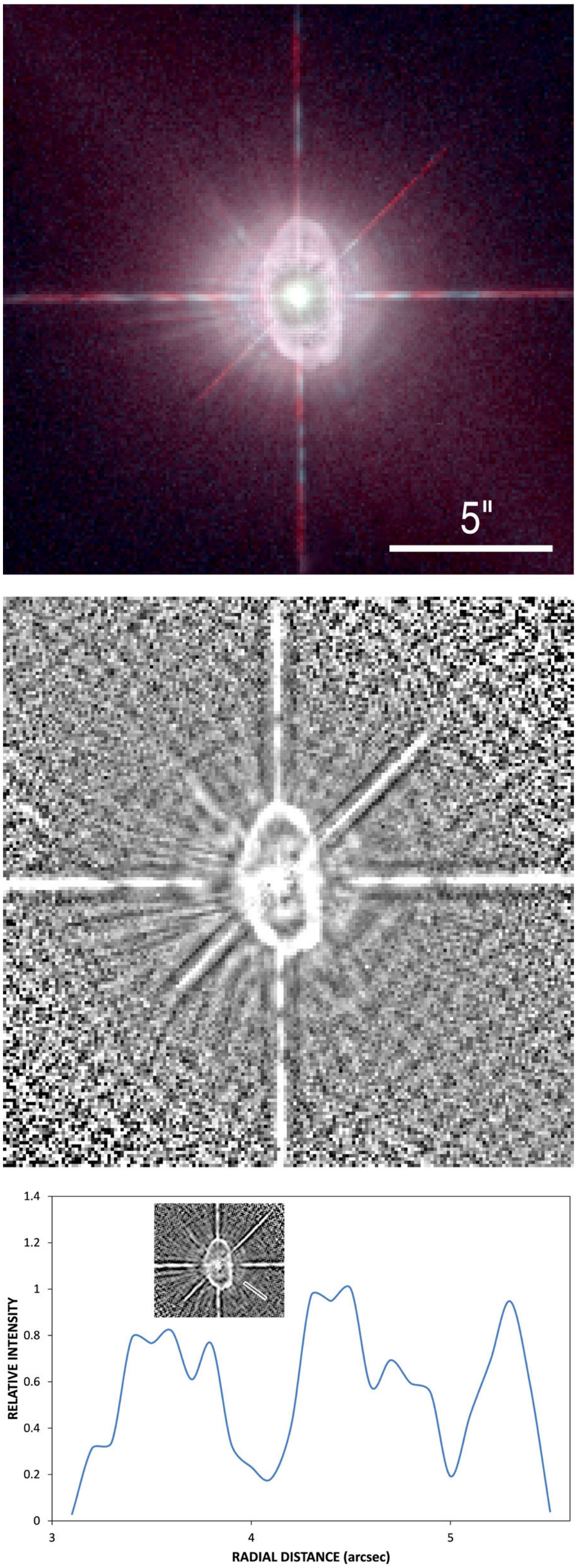

Figure A5. Same as Fig. 1 for HD 161796. The *HST* colour composite unsharp picture (top) includes the *F*547*M* (red) and *F*410*M* (green-blue) broad-band images. The sda image (middle) and profile (bottom) correspond to the *HST F*547*M* image.

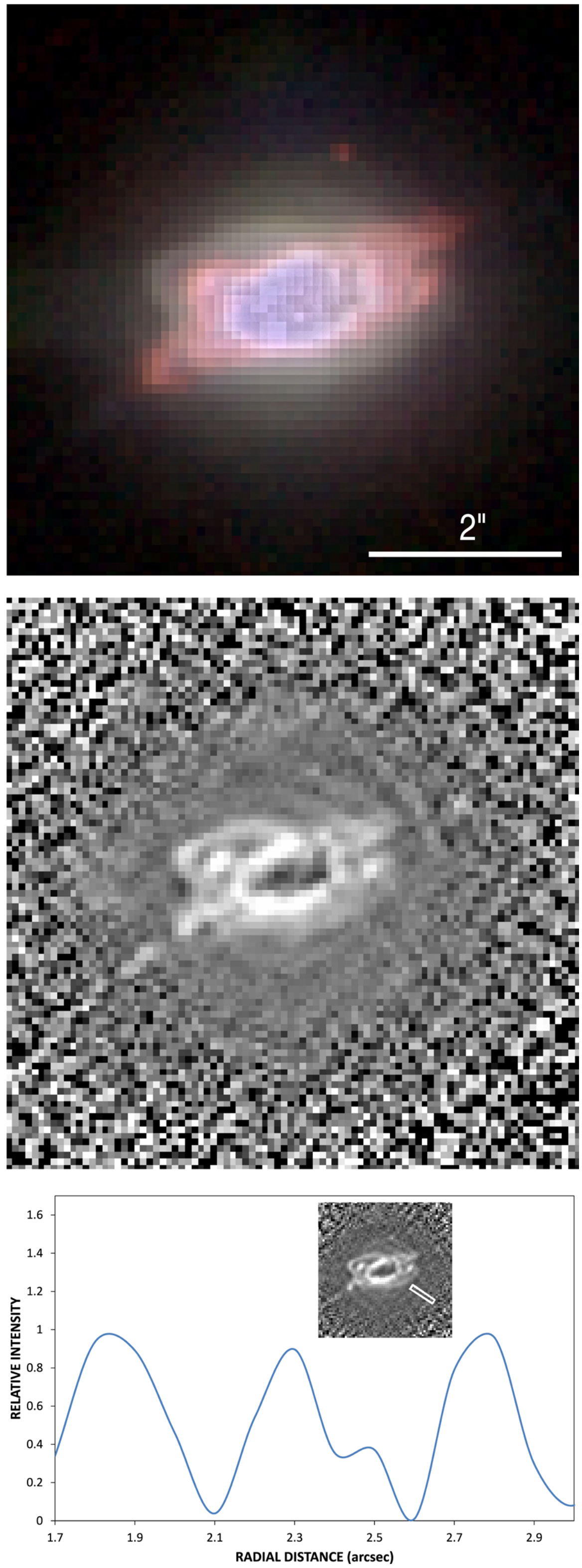

Figure A6. Same as Fig. 1 for IC 5117. The *HST* colour composite unsharp picture (top) includes the [N II] (red), Hα (green), and [O III] (blue) narrow-band images. The sda image (middle) and profile (bottom) correspond to the *HST* Hα image.

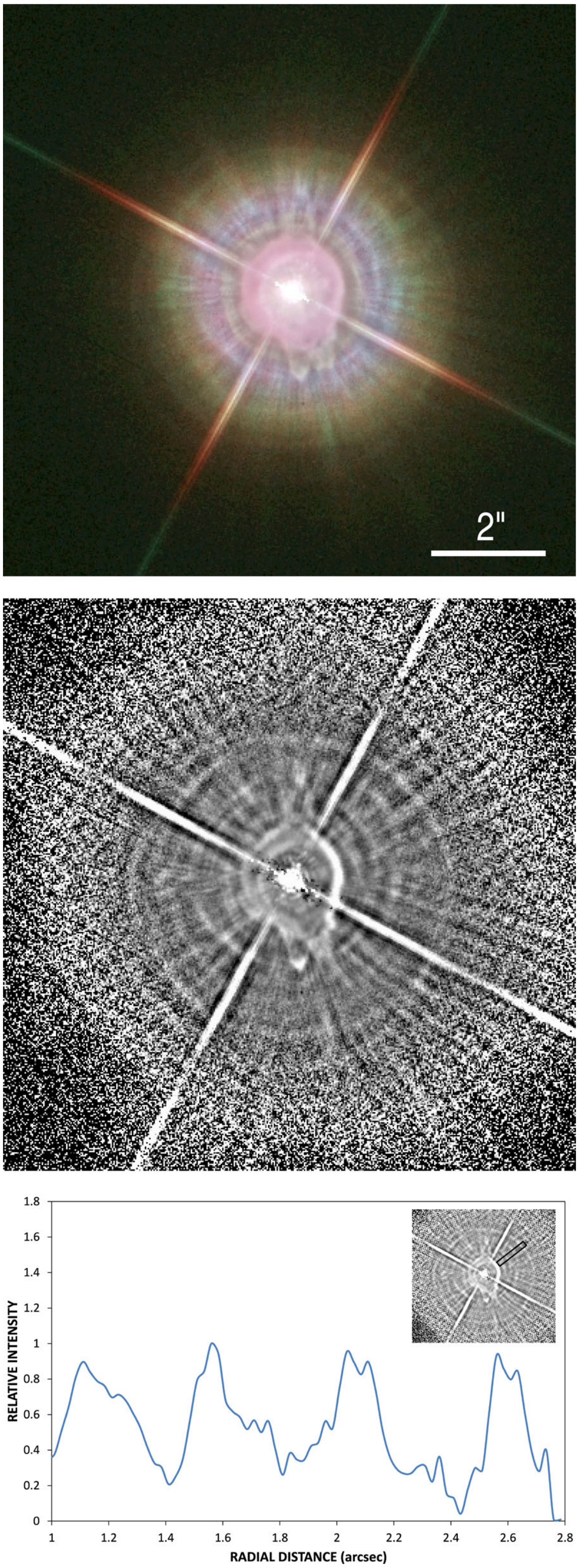

Figure A7. Same as Fig. 1 for GLMP 1058. The *HST* colour composite unsharp picture (top) includes the *F*606*W* (red) and *F*435*W* (green-blue) broad-band images. The sda image (middle) and profile (bottom) correspond to the *HST F*435*W* image.

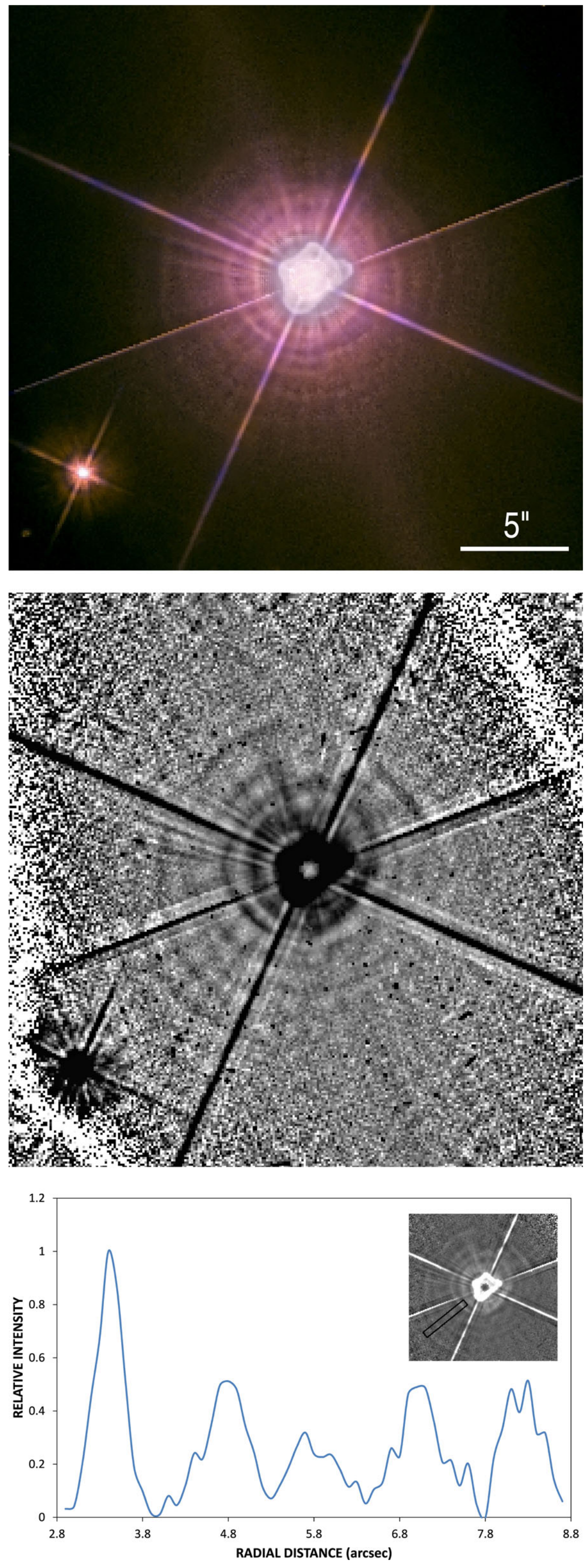

Figure A8. Same as Fig. 1 for GLMP 1059. The *HST* colour composite unsharp picture (top) includes the *F*814*W* (red) and *F*555*W* (green-blue) broad-band images. The sda image (middle) and profile (bottom) correspond to the *HST F*555*W* image.

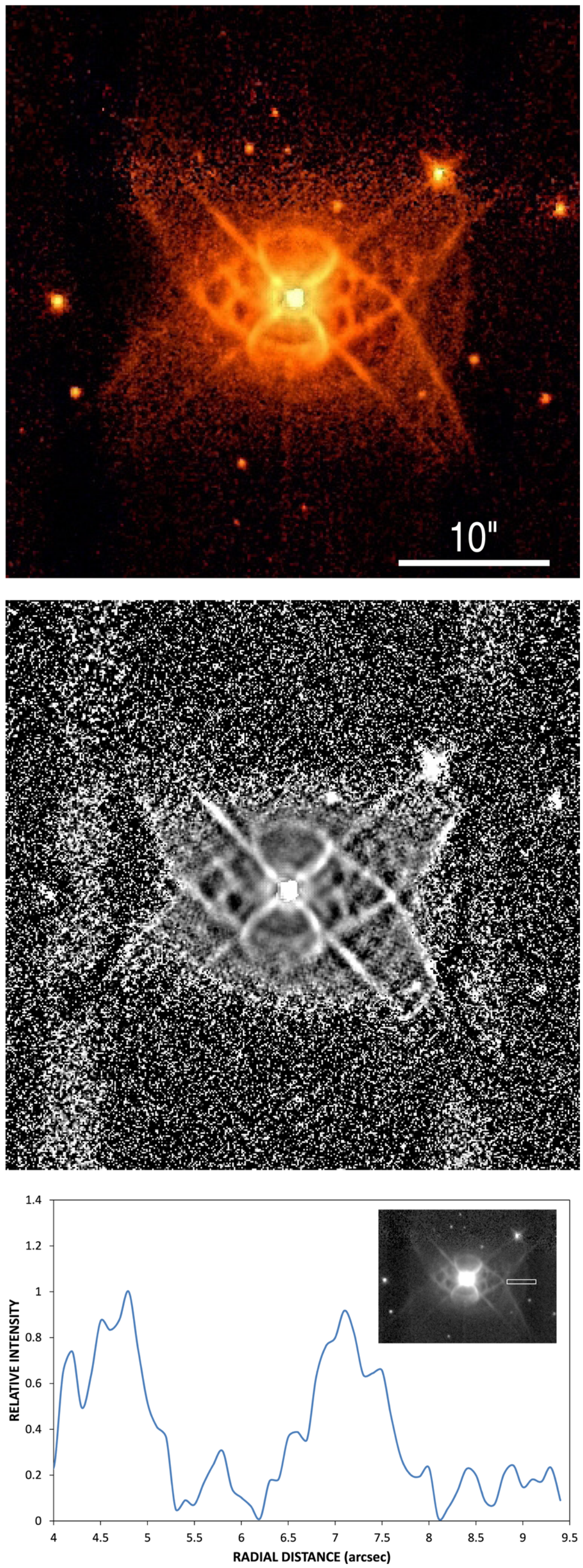

Figure A9. Same as Fig. 1 for Hb 12. The *HST* unsharp picture (top) includes only the NICMOS *F160W* (red) broad-band image. The sda image (middle) correspond to the *HST* NICMOS *F160W* image. The profile (bottom) was extracted from the direct image.

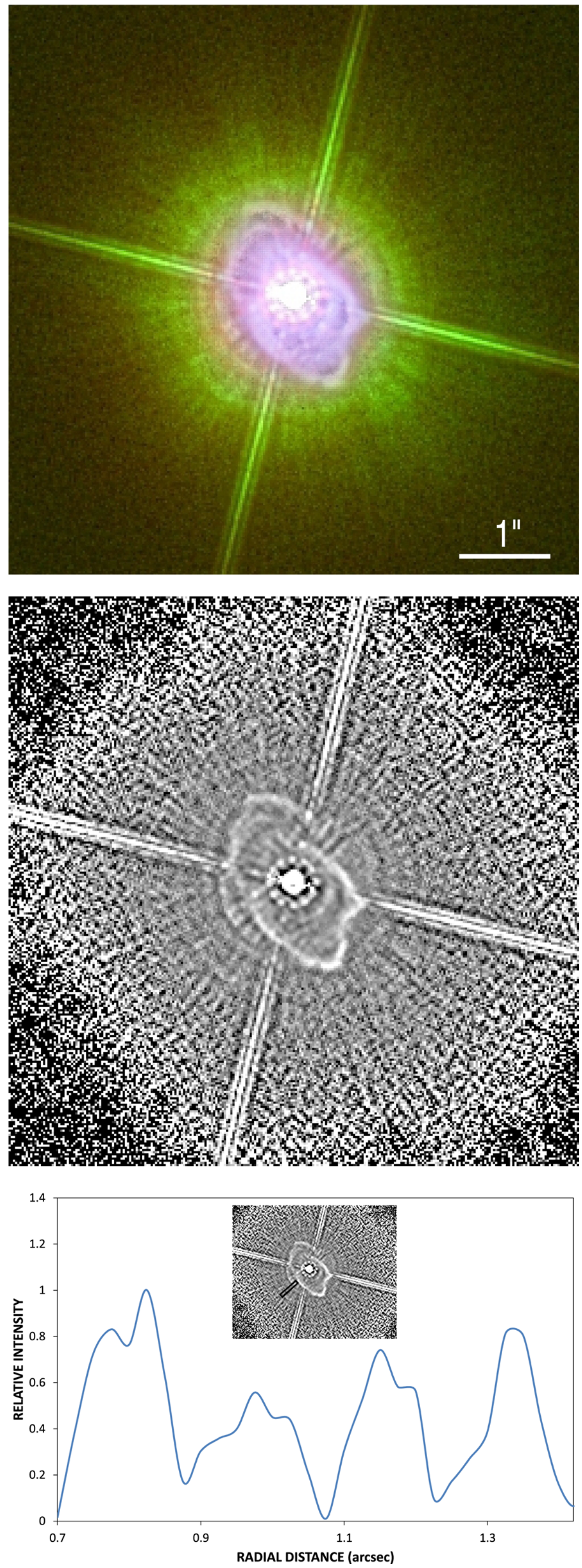

Figure A10. Same as Fig. 1 for M 2-47. The *HST* colour composite unsharp picture (top) includes the *F814W* (red) and *F606W* (green-blue) broad-band images. The sda image (middle) and profile (bottom) correspond to the *HST* *F606W* image.

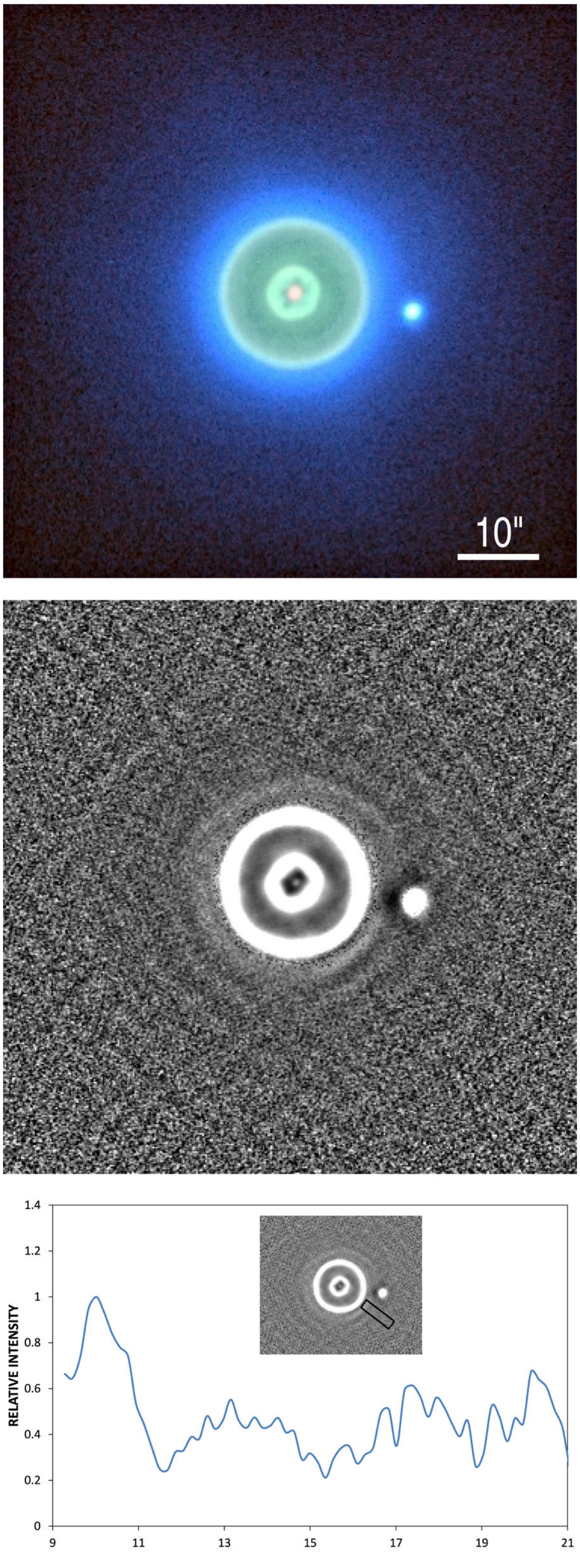

Figure A11. Same as Fig. 1 for the NOT images of IC 3568. The NOT colour composite unsharp picture (top) includes the [N II] λ6588 (red), Hα (green), and [O III] λ5007 (blue) narrow-band images. The sda image (middle) and profile (bottom) correspond to the NOT [O III] image.

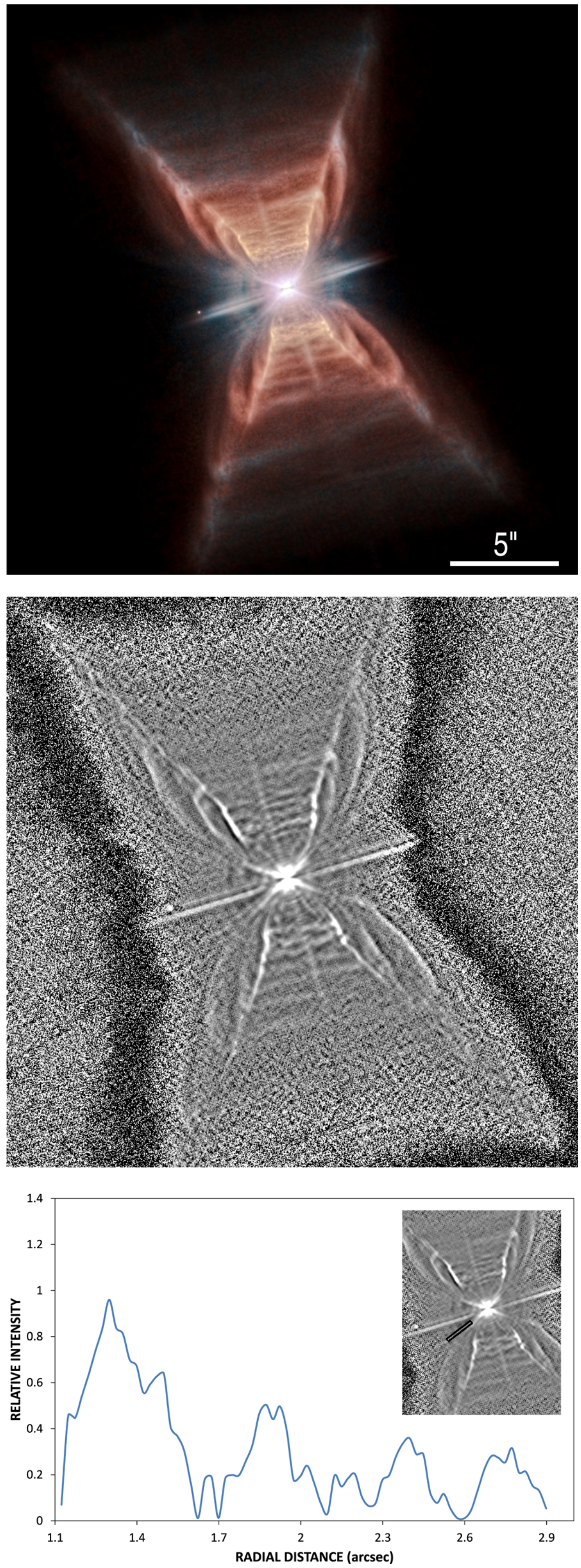

Figure A12. Same as Fig. 1 for CRL 915 (the red rectangle). The *HST* colour composite unsharp picture (top) includes the *F625W* (red–green) and [N II] (blue) images. Note that the colour criterium for the unsharp picture is different to that used for the other sources. The sda image (middle) and profile (bottom) correspond to the *HST* [N II] image.

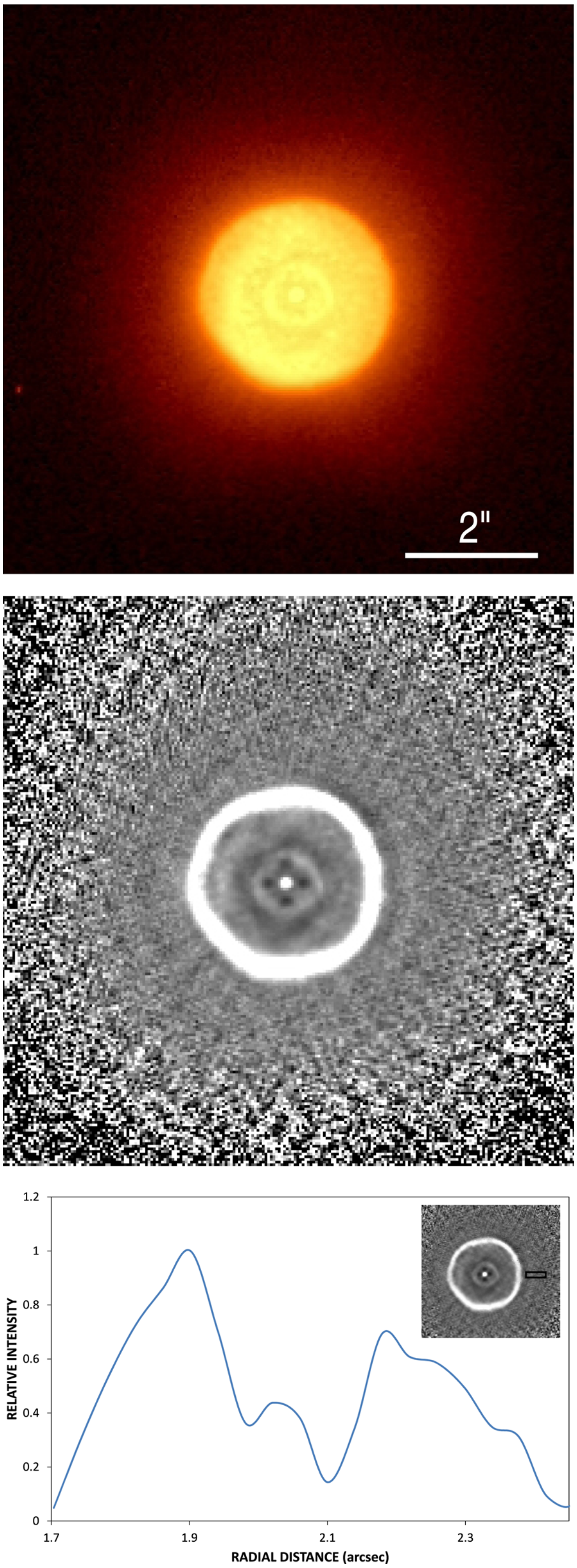

Figure A13. Same as Fig. 1 for Hen 2-5. The *HST* unsharp picture (top) includes only the [O III] (red) narrow-band image. The sda image (middle) and profile (bottom) correspond to the *HST* [O III] image.

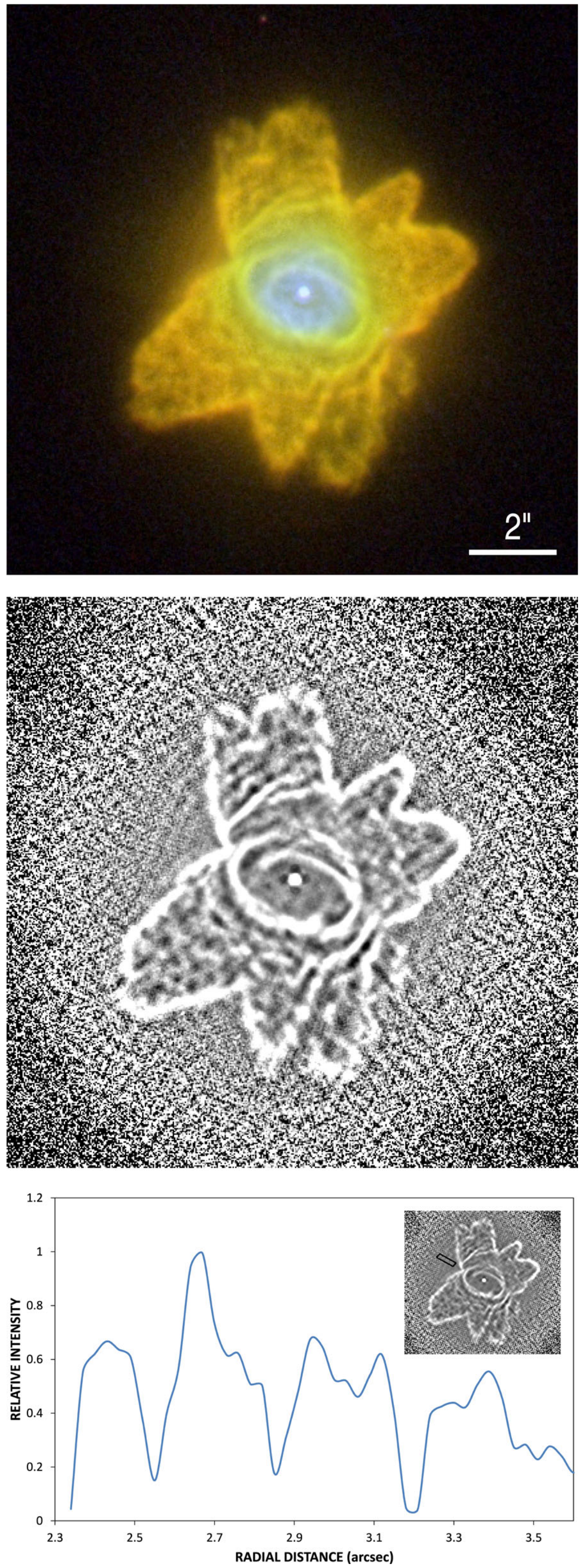

Figure A14. Same as Fig. 1 for Hen 2-47. The *HST* colour composite unsharp picture (top) includes the [N II] (red), Hα (green), and [O III] (blue) narrow-band images. The sda image (middle) and profile (bottom) correspond to the *HST* [N II] image.

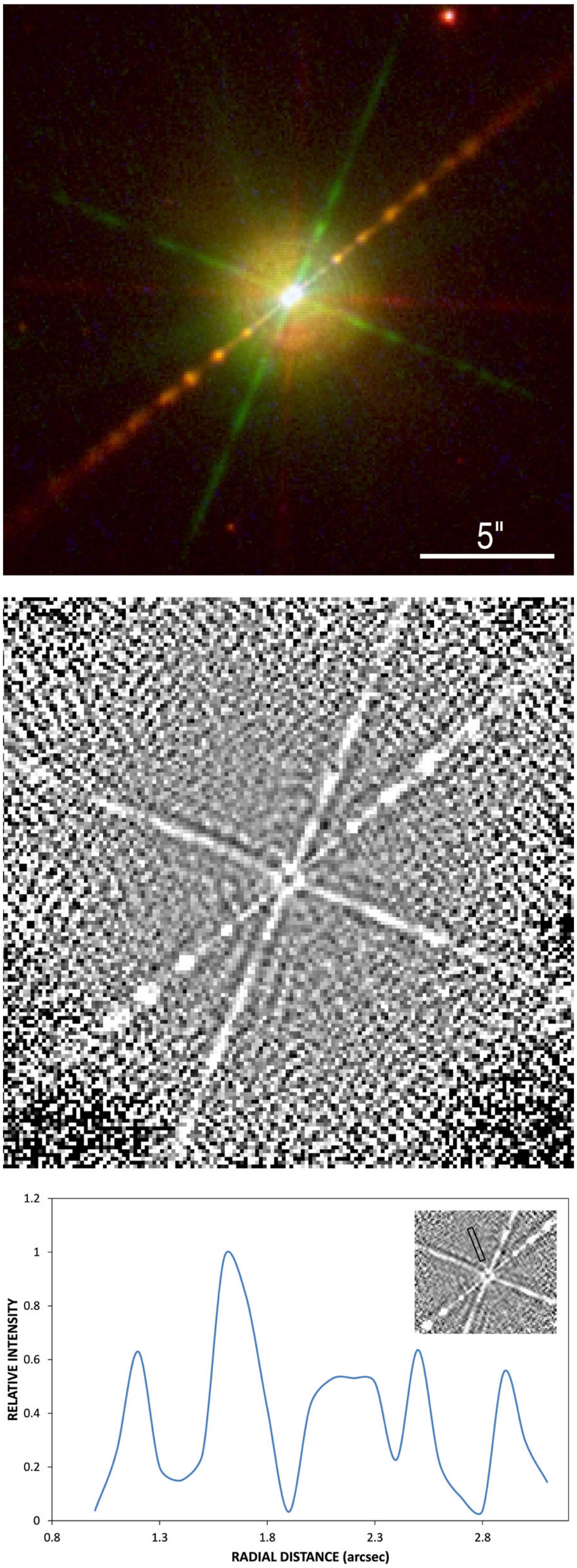

Figure A15. Same as Fig. 1 for Hen 2-90. The *HST* colour composite unsharp picture (top) includes the [N II] (red), Hα (green), and [O III] (blue) narrow-band images. The sda image (middle) and profile (bottom) correspond to the *HST* Hα image.

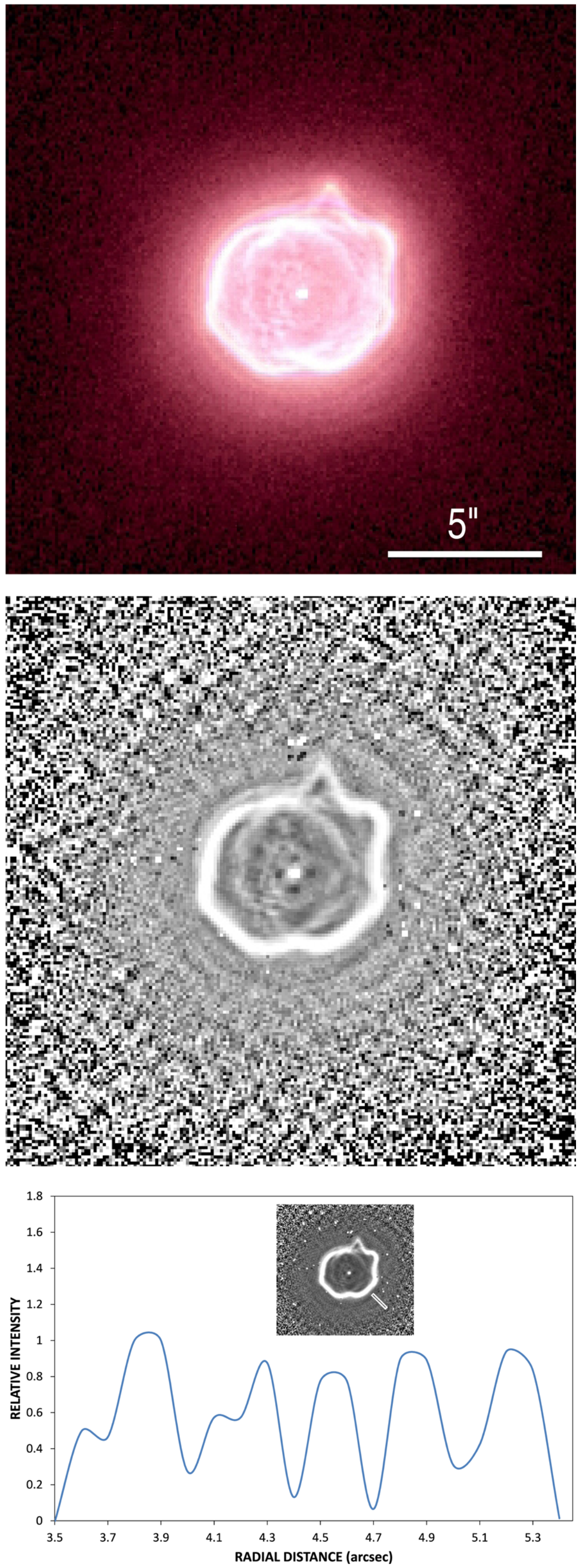

Figure A16. Same as Fig. 1 for Hen 2-131. The *HST* unsharp picture (top) includes only the Hα (red) narrow-band image. The sda image (middle) and profile (bottom) correspond to the *HST* Hα image.

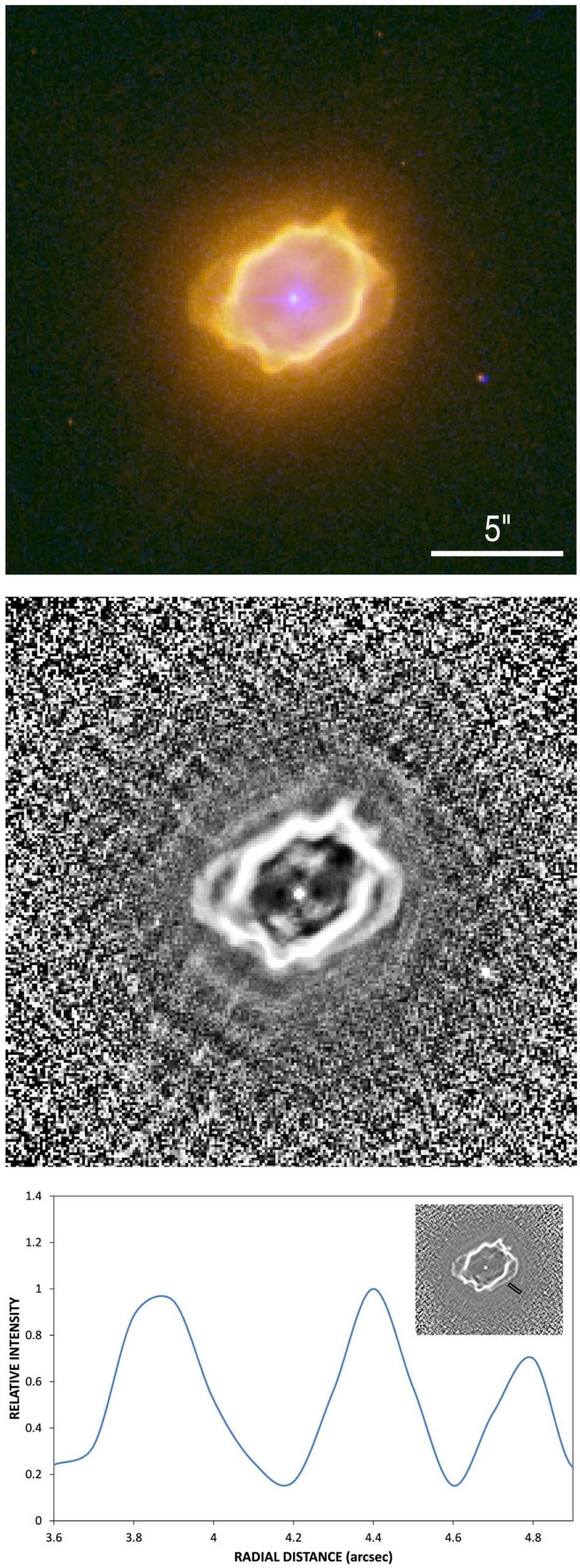

Figure A17. Same as Fig. 1 for Hen 2-138. The *HST* colour composite unsharp picture (top) includes the Hα (red) and *F555W* (green-blue) images. The sda image (middle) and profile (bottom) correspond to the *HST* Hα image.

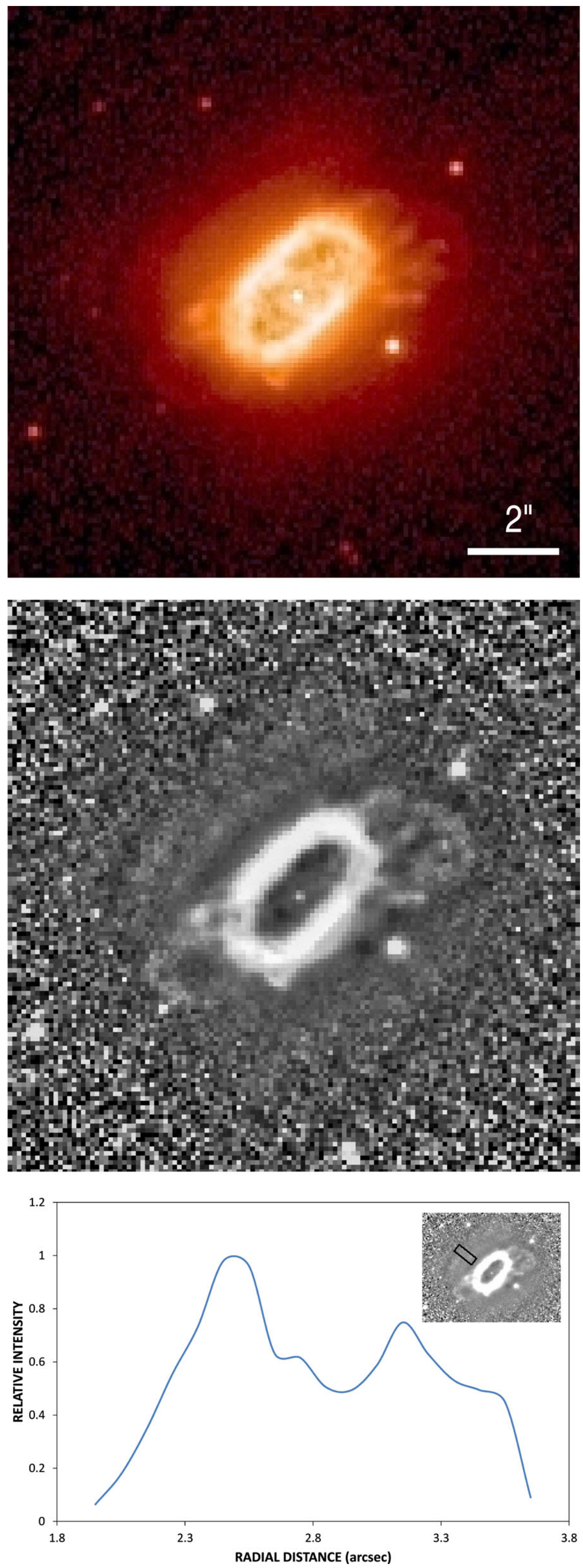

Figure A18. Same as Fig. 1 for Hen 2-142. The *HST* unsharp picture (top) includes only the Hα (red) narrow-band image. The sda image (middle) and profile (bottom) correspond to the *HST* Hα image.

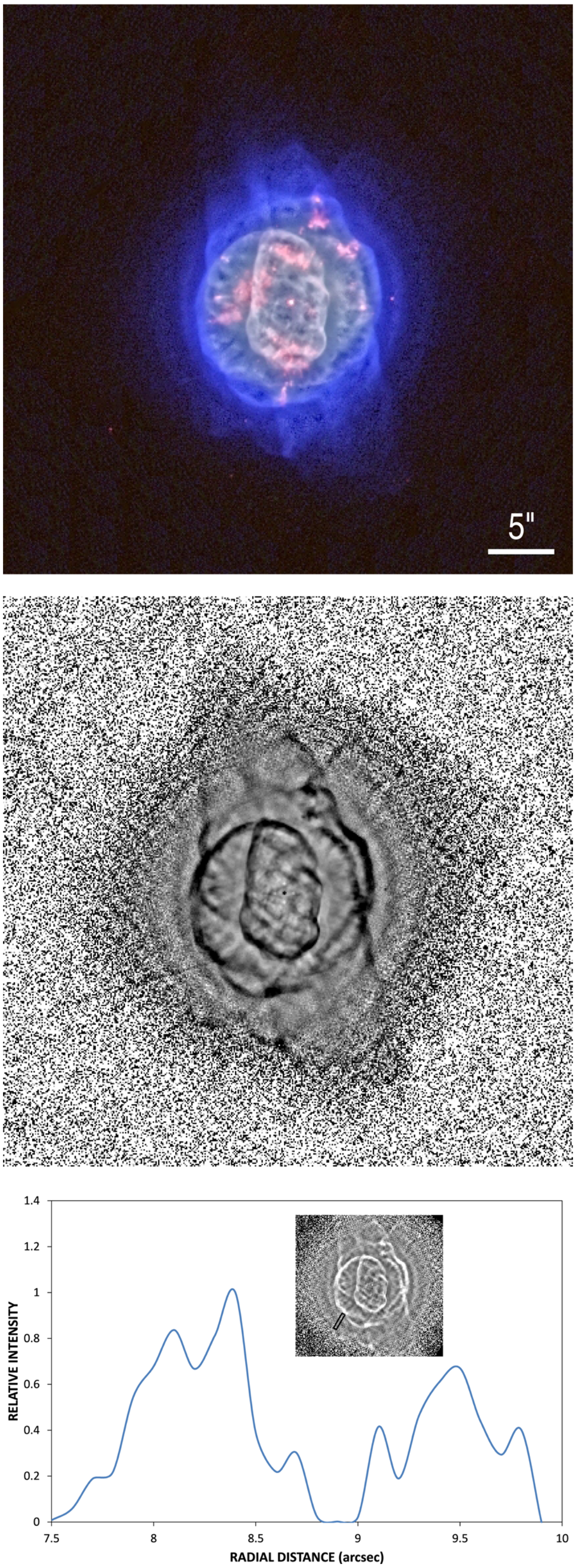

Figure A19. Same as Fig. 1 for NGC 5882. The *HST* colour composite unsharp picture (top) includes the [N II] (red), Hα (green), and [O III] (blue) narrow-band images. The sda image (middle) and profile (bottom) correspond to the *HST* [O III] image.

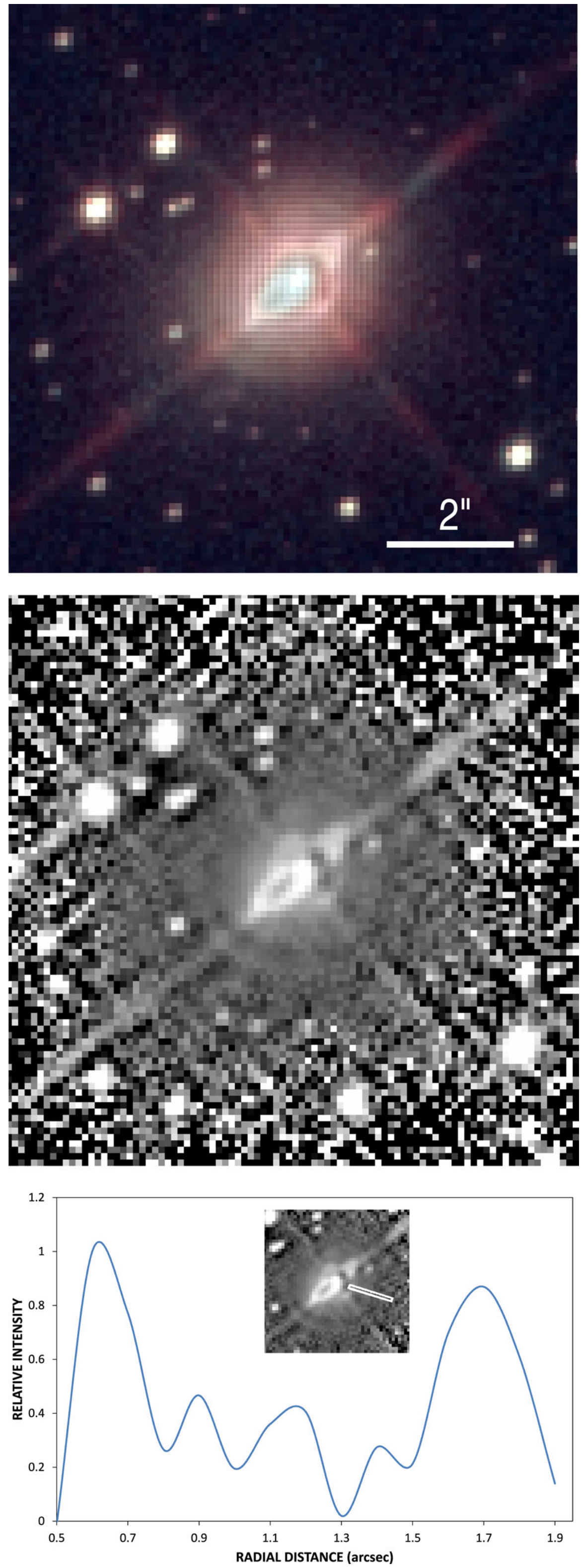

Figure A20. Same as Fig. 1 for GLMP 531. The *HST* colour composite unsharp picture (top) includes the *F*814*W* (red) and *F*606*W* (green-blue) broad-band images. The sda image (middle) and profile (bottom) correspond to the *HST* *F*606*W* image.

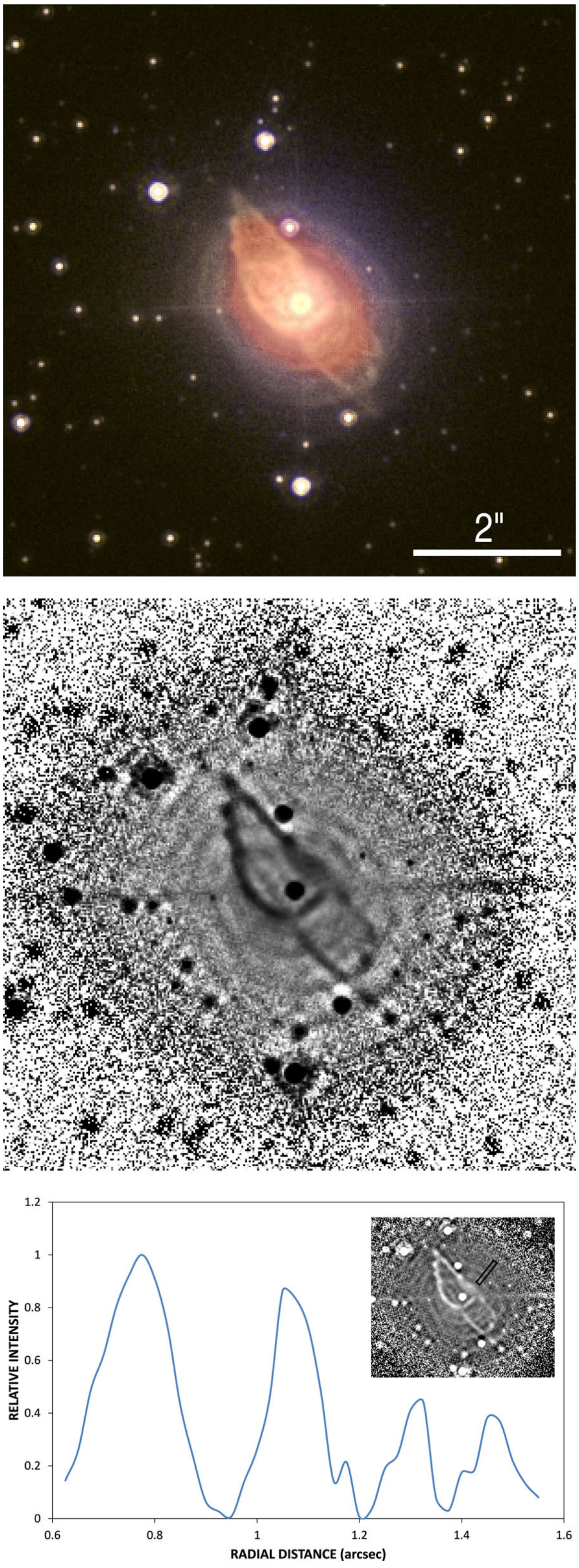

Figure A21. Same as Fig. 1 for PM 1-176. The *HST* colour composite unsharp picture (top) includes the *F*814*W* (red) and *F*606*W* (green-blue) broad-band images. The sda image (middle) and profile (bottom) correspond to the *HST F*606*W* image.

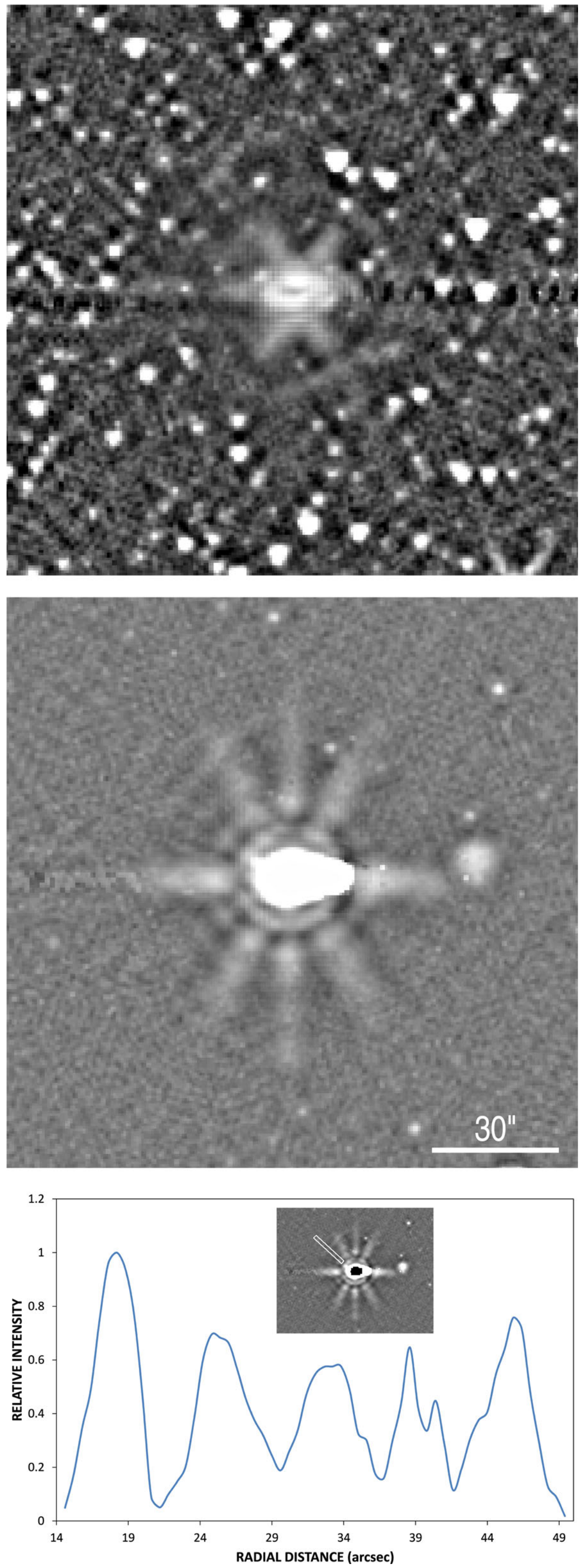

Figure A22. *Spitzer* IRAC 3.6 μm (top) and 8 μm images of NGC 6572. An outer arc is clearly visible in the 3.6 μm image. (Bottom) IRAC 8 μm sda profile through the halo ring structures.

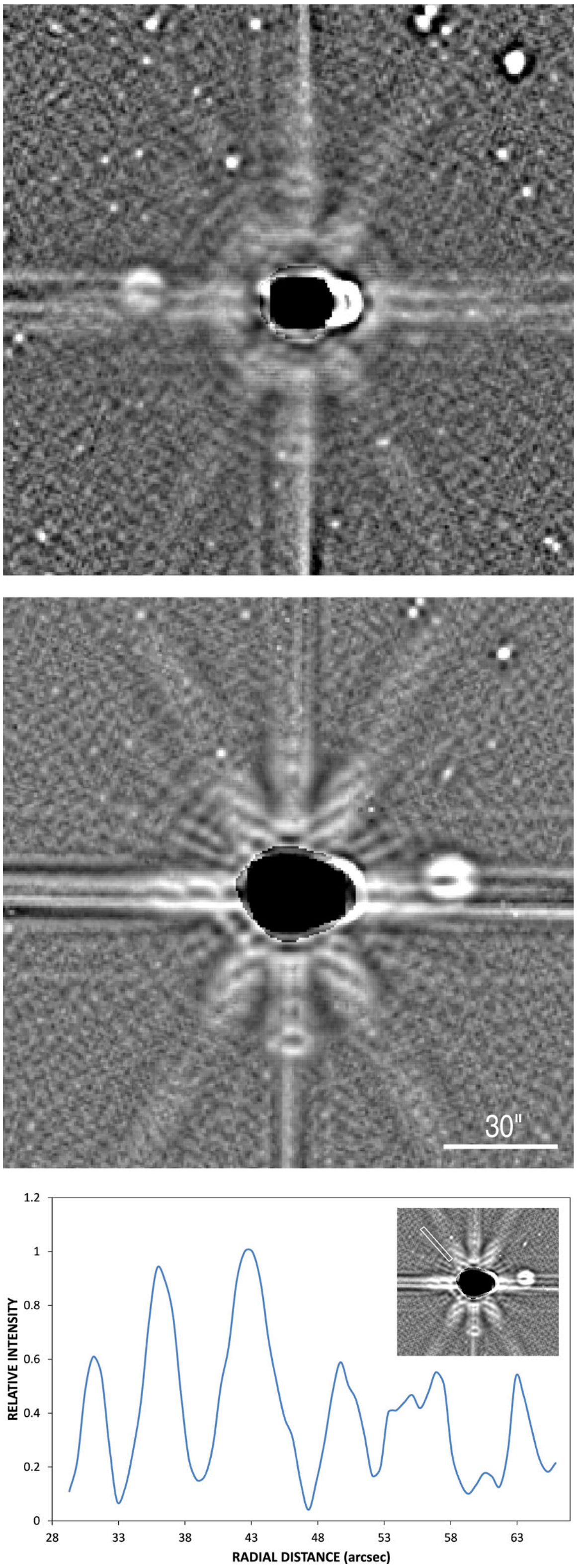

Figure A23. Same as Fig. A22 for NGC 7027. The rings in the 8 μm image resembles the *HST* image by Su (2004).

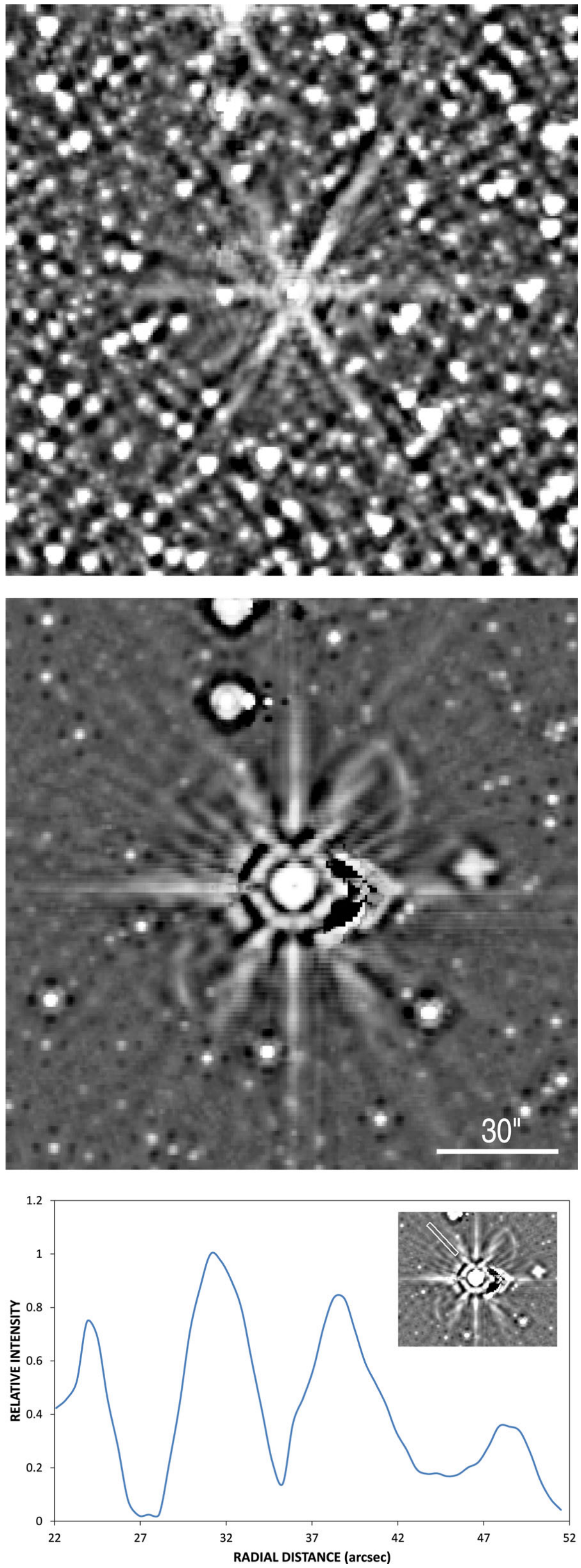

Figure A24. Same as Fig. A22 for Mz 3.

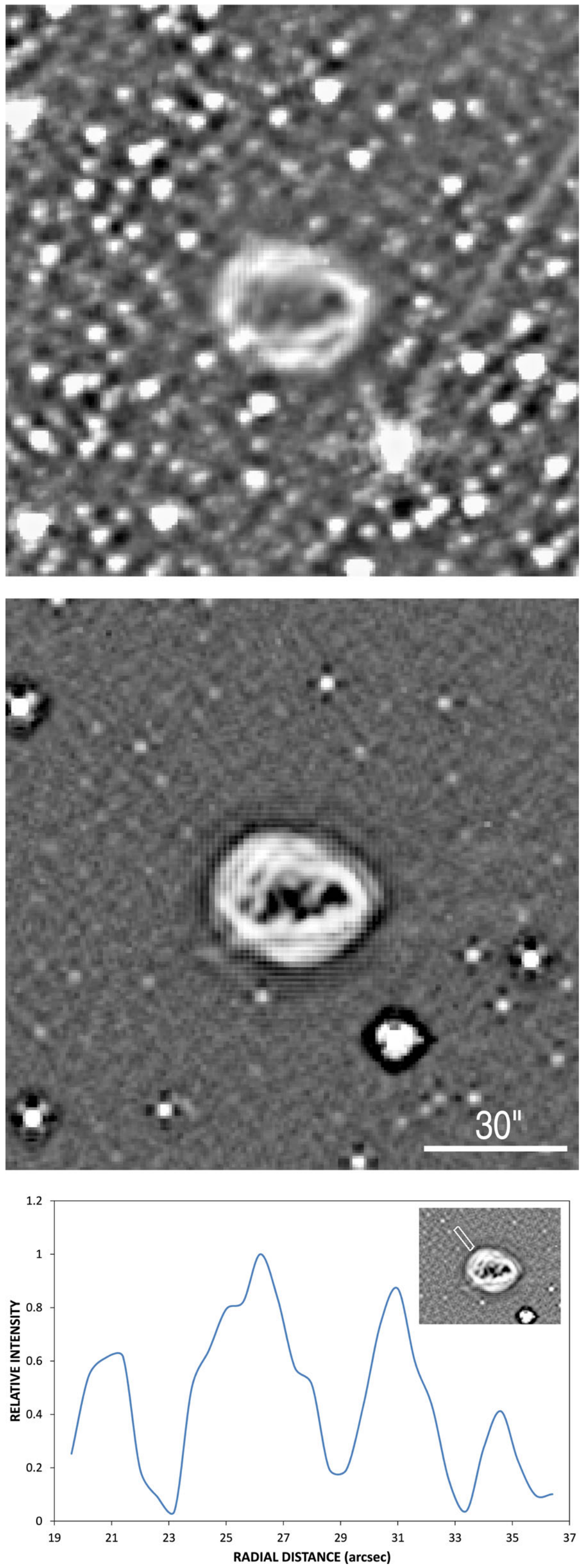

Figure A25. Same as Fig. A22 for NGC 6153.

This paper has been typeset from a TEX/LATEX file prepared by the author.